UNIVERSITY OF CALIFORNIA
RIVERSIDE

Post-Growth Manipulation of Transition Metal Dichalcogenides Thin Film

A Dissertation submitted in partial satisfaction
of the requirements for the degree of

Doctor of Philosophy

in

Materials Science and Engineering

by

Quan Ma

August 2014

Dissertation Committee:
Dr. Ludwig Bartels, Chairperson
Dr. Yadong Yin
Dr. Cengiz Ozkan

The Dissertation of Quan Ma is approved:

_____

_____

_____

Committee Chairperson

University of California, Riverside

ACKNOWLEDGEMENTS

I would like to thank my advisor, Ludwig Bartels, for his excellent guidance, patience and providing me this incredible opportunity to do research in his lab.

Dr. Bartels works very hard and teaches us himself by examples. He is extremely patent and kind whenever I got confused in a question or an experimental result, he was always able to point out the problem and put me back on the right track. His knowledge in physics and chemistry helped me understand many novel phenomena we observed in our experiment and his experienced and creative thoughts help me gain more insights. I want to thank him for defining a good example of a good researcher. From him, I learned the way to do research and the way to be a good mentor of others.

I want to thank Professor Cengiz Ozkan and Professor Yadong Yin for serving on my advancement and doctoral committees. I took a nanoscale science and engineering course from Professor Ozkan that turned out to be very useful to me as well as my research projects in Bartels' lab. I also had several insightful discussions with Professor Yarmoff in the context of the surface science seminar regarding the research that I was interested in.

I had the pleasure to overlap with these people in Dr. Bartels' group at different times: Zhihai Cheng, Greg Pawin, Dezheng Sun, John, Mann, John Wyrick, Edwin Preciado, Miguel Isarraraz, Chen Wang, Dae-Ho Kim, Yeming Zhu, Miaomiao Luo, Jon Wyrick, Wenhao Lu, Sarah Bobek, Koichi Yamaguchi, Tai Tran, Michelle Wurch, Velveth Klee, David Barroso, Ariana Nguyen, Sahar Naghibi, Eva Bonilla, Gretel von Son, Andrew Nguyen, Mark Micklich and Jessica McKinley. I learned many useful

techniques and skills from senior group members. Later, as I became more experienced, I transferred my knowledge to the new members of the group.

Last, I want to thanks my Parents, for bring me to this world, for all of the sacrifices that they have made for me, for all that they are doing in order to build a brighter tomorrow for me.

ABSTRACT OF THE DISSERTATION

Post-Growth Manipulation of Transition Metal Dichalcogenides Thin Film

by

Quan Ma

Doctor of Philosophy, Graduate Program in Materials Science and Engineering
University of California, Riverside, August 2014
Dr. Ludwig Bartels, Chairperson

The intense interest in graphene as the prototype 2D electronic material has recently been complemented by the investigation of layered transition metal dichalcogenides (TMD), notably MoS_2 and $MoSe_2$. These materials provide the favorable mechanical properties of graphene, but exhibit a direct bandgap without the need for nanostructuring, [1, 2] chemical functionalization, [3] or the application of a strong electric field to bilayers. As a monolayer, MoS_2 becomes a direct-gap semiconductor with a gap of 1.8 eV [4]. In this dissertation, X-ray photoelectron spectroscopy (XPS), photoluminescence spectroscopy and high-resolution angle resolved photoemission spectroscopy (ARPES) have been used to investigate monolayer and alloy thin films grown on various substrates. My research focuses on the thin film modification and characterization, composition analysis, low-energy argon ion sputtering process and bandgap tuning.

Table of Content

Table of Figures

Chapter 1 Introduction and Overview

1.1 Overview

Transition Metal Dichalcogenides (TMD) thin films have attracted strong attention as a material that can be prepared in a stable form down to the single-layer limit while at the same time maintaining interesting electronic and catalytic properties[5]. The development of electronic, spintronic and photonic devices based on TMD thin film materials is important due to the potential tuning ability and excellent physical and chemical properties of TMD thin films [6].

My research projects focused on studying the manipulation of the bandgap of single-layer MoS_2 with a sputtering-based method. I was also a major contributor in several other experiments while collaborating with different research groups. I have been in charge of constructing three vacuum systems: a low temperature XPS system with VG Scienta R3000 Analyzer, a low temperature XYZ manipulator and a photoluminescence spectroscopy.

1.2 Instruments

1.2.1 Low Temperature X-ray and Ultraviolet Photoelectron Spectroscope

I designed and assembled an UHV XPS/UPS system with a commercial VG Scienta R3000 analyzer, TX400 X-ray source and an UV source. This system also has much additional equipment: mass spectrometer, metal evaporator, XYZ sample

manipulator, liquid molecule dosing valves, sample heaters and sample cooling.

I also designed and built a sample load-lock system to transfer samples faster and a quick pumping chamber that significantly reduces the time of XPS measurements. On this XPS system, I have developed two methods for modifying properties of TMD thin films: (1) Use low-energy argon ion beam sputtering to selectively remove the sulfur content without significant depletion of molybdenum. (2) Characterize the substitution process for S/S and S/Se replacement by using thin film recovery and modification techniques.

Other experiments that can be conducted using this system are: TMD thin film growth, TPD spectroscopy, PL measurements, etc.

1.2.2 Photoluminescence Spectroscope

I installed a photoluminescence spectroscope for the use with the UHV XPS system. I used a wavelength of 532nm Spectra Physics Millenia green laser with a 1200 lines mm^{-1} 750nm grating spectrometer and a liquid-nitrogen cooled Princeton Instruments SPEC-10 CCD detector. For in situ measurements, a 50-mm focal length lens inside the UHV system was used to focus about 100 mW of pump beam onto the sample surface with a spot of ~100 μm. The measurements include the investigation of the in situ reaction of TMD thin films under different modification methods.

1.2.3 XYZ manipulator

I designed and built a XYZ sample manipulator. This manipulator allows us to easily move devices in the UHV chamber to achieve in situ measurements of low temperature I-V experiments. It contains three step motors for the sample stage movement, 10 coaxial cables/ 2 thermo couples for signal transfer, the cooling system, the special TMD thin film device holder and the TPD sample holder. By using this system, we can do the UHV level low temperature in situ I-V measurements and TPD experiments for different TMD devices.

1.3 Research

Chapter 2 discusses the principle of the X-ray Photoelectron Spectroscope and the designing process of how to construct the XPS, PL and XYZ manipulator system. Chapter 2 also describes the sample preparation of the TMD thin film growth.

Chapter 3 illustrates the sputtering process of MoS_2 thin films by low-energy argon ions. It can selectively reduce the sulfur content of the material without significant depletion of molybdenum. XPS shows little modification of the Mo 3d states during this process, suggesting the absence of significant reorganization or damage to the overall structure of the MoS_2 film. Measurements of the photoluminescence at temperatures between 175 and 300 K show quenching of almost 80% for ~10% decrease in sulfur content.

Chapter 4 demonstrates the methods of bandgap tuning of single-layer MoS_2

film on SiO2/Si via substitution of its sulfur atoms by selenium through the process of gentle sputtering, exposure to a selenium precursor, and annealing. Photoluminescence and X-ray photoelectron spectroscopy provide direct evidence of optical band gap shift and selenium incorporation, respectively. The resultant films are stable in vacuum, but deteriorate under optical excitation in air.

Chapter 5 discusses the $MoS_{2(1-x)}$ Se_{2x} single-layer films that are prepared using a mixture of organic selenium and sulfur precursors as well as a solid molybdenum source. The direct bandgaps are found to scale nearly linearly with composition in the range of 1.87 eV (pure single-layer MoS_2) to 1.55 eV (pure single-layer $MoSe_2$), permitting straightforward bandgap engineering.

Chapter 6 discusses the areas of single-layer MoS_2 films prepared under CVD condition. The films were characterized by means of Raman spectroscopy, photoluminescence, low-energy electron diffraction and microscopy, and XPS and mapping.

Chapter 7 describes the work done in Hiroshima, Japan. We found a wave vector dependence of the band symmetries for MoS_2(0001) in angle-resolved photoemission. The band structures are found to be significantly different for states of even and odd reflection parities, despite the absence of true mirror plane symmetry away from Γ point, the Brillouin zone center, along the line to the K point, at the Brillouin zone edge. Our measurements agree with the density functional theory (DFT) calculation for each band symmetry, with a notable exception of the Mo $4d_{x2-y2}$ contributions to the valence band structure of

MoS_2(0001). The band structure is indicative of strong S 3p and Mo 4d hybridization. In particular, the top of the valence band is strongly dominated by Mo $4d_{3z2\text{-}r2}$ derived states near Γ, whereas near K Mo $4d_{x2\text{-}y2}$ as well as Mo $4d_{xy}$ dominates. In contrast, the bottom of the valence band is dominated by Mo 5s and S 3pz contributions.

Chapter 2 X-ray Photoelectron Spectroscope System

2.1 Introduction

XPS, also known as ESCA (Electron Spectroscopy for Chemical Analysis), is the electron spectroscopy that measures the elemental composition of a solid sample surface (normally within ~10 nm).

It can be used to identify and quantify elemental composition with all elements except hydrogen or helium. XPS requires high vacuum (~10^{-8} mbar) or ultra-high vacuum (~10^{-9} mbar) conditions.

XPS is widely used to determine: the chemical or electronic state (binding energy) of each element in the surface, the thickness down to few layers (1-8 nm), of -the material, the density of electronic states, compositional mapping, empirical formula as well as the composition of the solid target materials.

Relative quantitative elemental analysis is another important job that XPS can achieve. The quantitative accuracy depends on the signal-to-noise ratio, peak intensity, accuracy of relative sensitivity factors, correction for electron transmission function, surface volume homogeneity, etc.

XPS is routinely used to analyze inorganic compounds, metal alloys, semiconductors, polymers, elements, and many others, but less routinely used for the hydrated forms of materials

2.2 Physics of XPS

Initially, an input photon from the source hits the electron from an atom. This process happens without the energy loss since photons have zero rest mass. The result of this process is the emission of the electron directly from the atom. Then the binding energy (B.E.) of the electron can be calculated by the measurement of the kinetic energy (K.E.)[7].

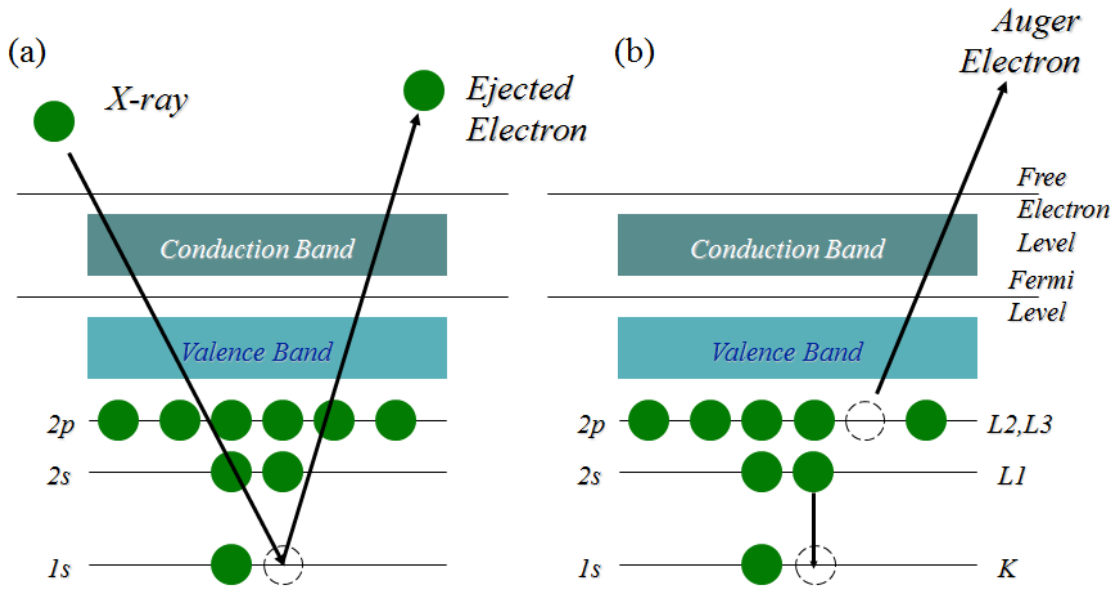

Figure 2-1: (a) One electron with certain binding energy is ejected by the incident x-ray electron. Above the free electron level, the electron is free from the atom. (b) A hole is created by this process in the 1s level. An electron from the 2s level fills in the 1s hole and the transition energy is imparted to a 2p electron that is emitted. It is called the Auger electron.

The B.E. is characteristic of the core electrons for each element. It is determined by the attraction of the electrons to the nucleus. If an electron with

certain energy is pulled away from the nucleus, the attraction between the electron and the nucleus decreases and the B.E. decreases. Eventually, there will be a point when the electron will be free of the nucleus[8].

The B.E. can construct the spectrum since the K.E. is dependent on the X-ray energy but B.E. is not. The input photon energy hν, kinetic energy and binding energy are related by this equation: $B.E. = h\nu - K.E. - \varphi_{spec}$.

φ_{spec} is the work function of the instrument, it is an adjustable instrumental correction factor that accounts for the few eV of K.E. given up by the photoelectron as it becomes absorbed by the instrument's detector. It is a constant that rarely needs to be adjusted in practice.

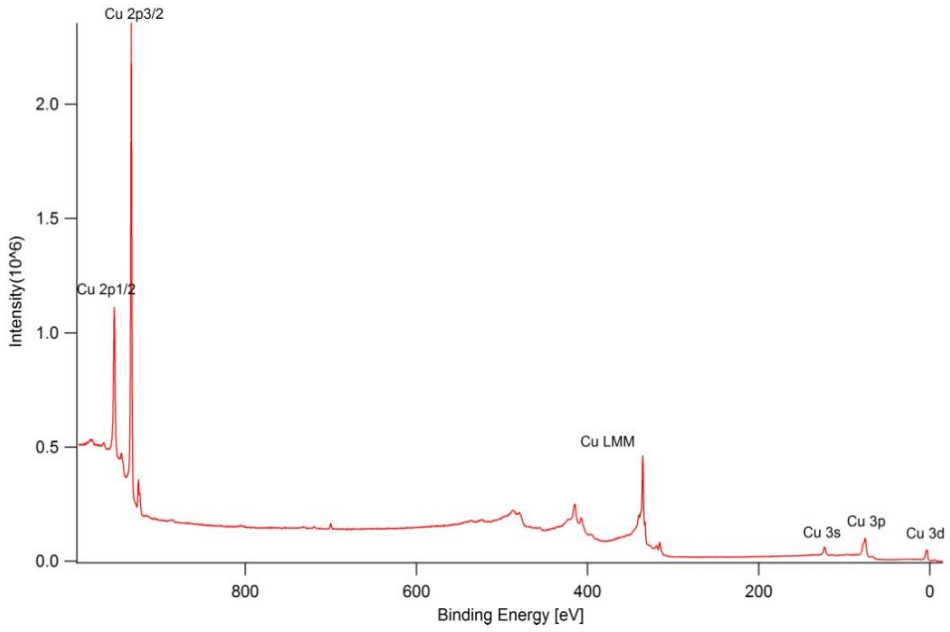

Figure 2-2: XPS spectrum of cleaned Cu (111) surface

Fig. 2-2 is the survey spectrum of clean copper surface. The excitation energy is Al Kα (1486.6eV). It contains typical copper characteristic peaks: $2p_{1/2}$, $2p_{3/2}$,

LMM, 3s, 3p and 3d. Cu LMM is the Auger electron peak.

2.3 XPS System Design

The XPS instrument employs various pumping systems to achieve the Ultra High Vacuum (UHV) environment. To reach UHV condition, it needs special pumping systems and low outgassing chambers. The chamber must have low outgassing rate, low corrosion rate and low vapor pressure.

A typical vacuum system contains multiple pumps, valves and vacuum gauges to monitor the pressure [9]. The rough pump can pump out the chamber and reach about 10^{-3} Torr, and can support the turbo molecular pumps. The backing turbo pump can produce a pressure down to 10^{-10} Torr range after proper bake-out. Other pumping equipment includes: ion pump and titanium sublimation pump. These two kinds of pumps are not for initially pumping down. They should not be operated above about 10^{-5} Torr since their functions are trapping, pushing or ionized the molecules into the solid state to lower the pressure.

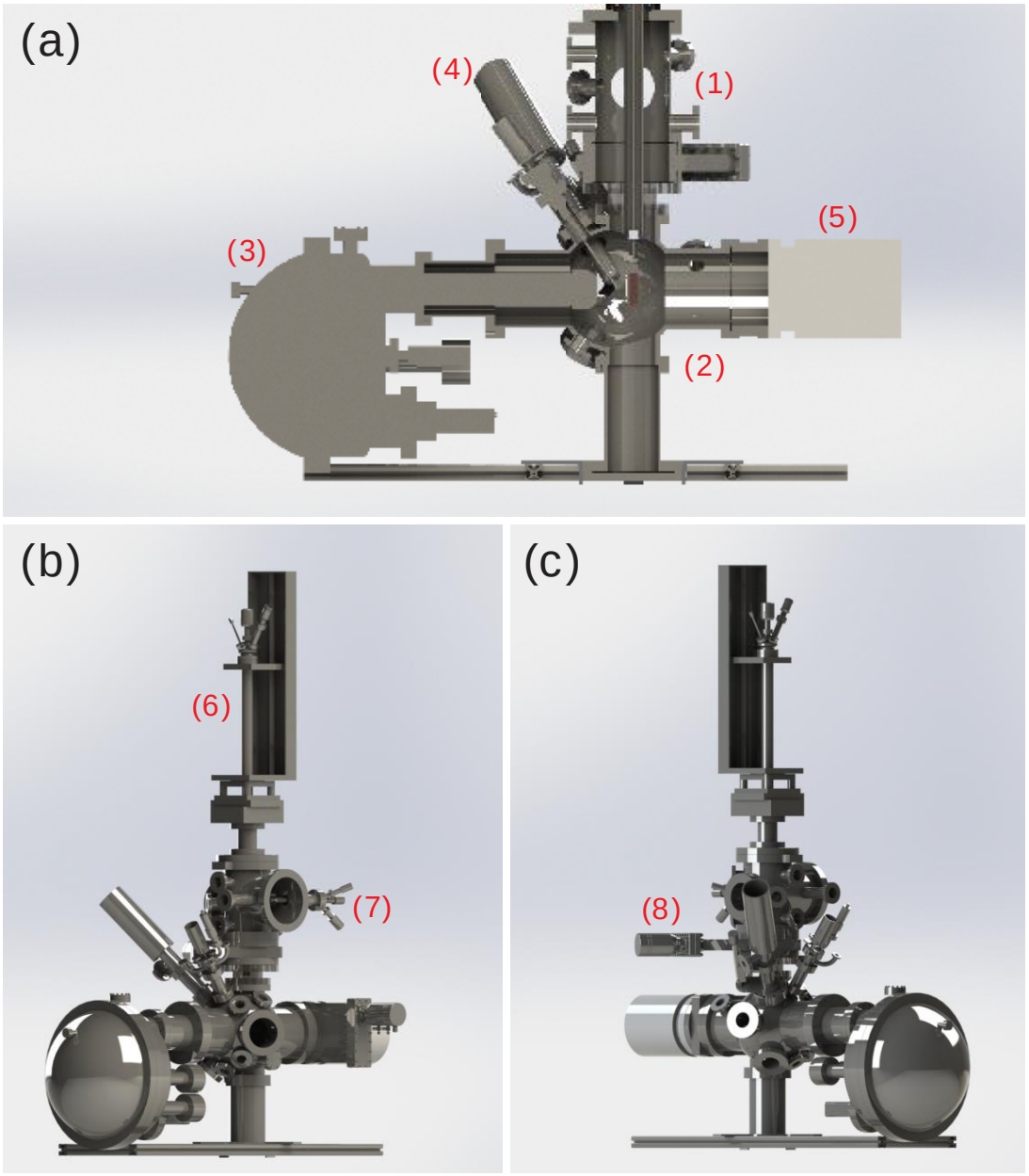

Figure 2-3: Solidworks model of the home built XPS. (a) Middle cross section image of the system. (b) and (c) Different view describes the UHV design.

The home built XPS contains (1) preparation chamber, (2) XPS chamber, (3) XPS analyzer, (4)X-ray/UV source, (5) turbo molecular pumps with rough pumps (6) manipulator, (7) E-beam evaporator and (8) different gate valves. Additionally, the system also has the ion gauge for the pressure monitoring, the mass spectrometer, the leak valve for molecule deposition, the load lock for quick sample loading, the ion pump and the sputter gun etc.

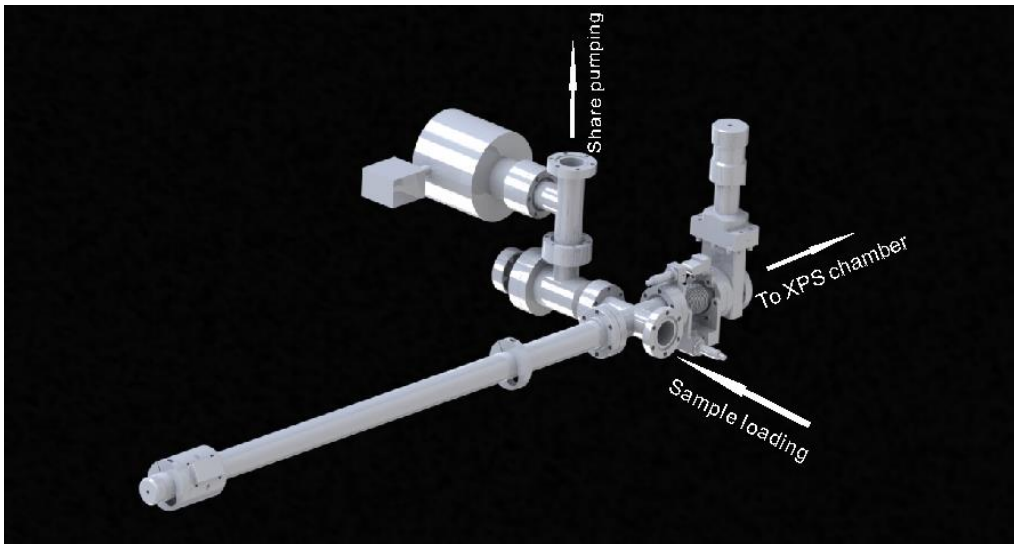

Figure 2-4: Load-lock component connected to the XPS chamber

The load-lock has a gate valve that connected to the main chamber, a transfer arm and a pumping system. This design allows quick sample loading from the side flange onto the transfer arm. So without breaking the pressure in the main chamber, the load-lock can be pumped out first than deliver the sample for the XPS measurements.

2.4 Other Instruments Design

2.4.1 Low Temperature XYZ Manipulator

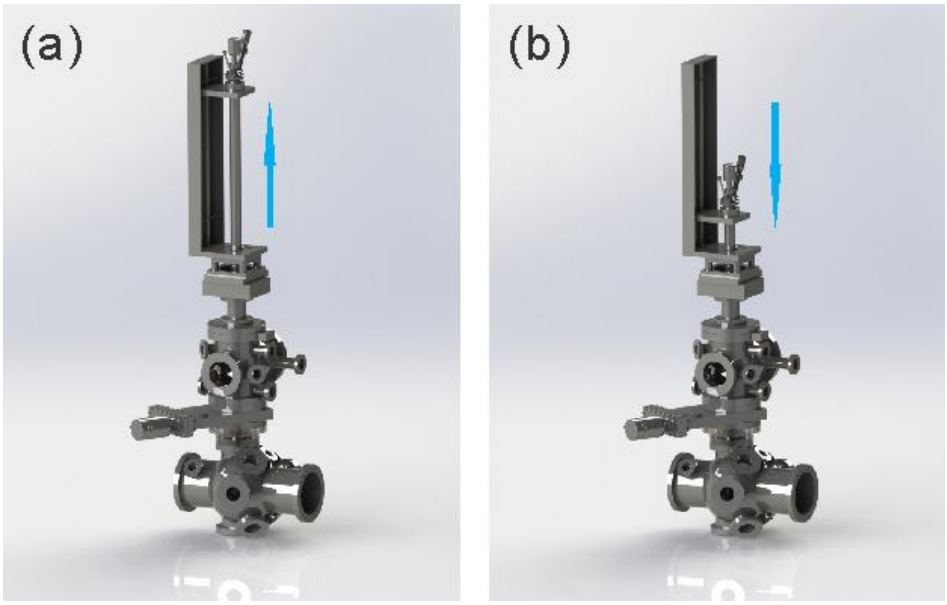

Figure 2-5: Solidworks model of XYZ manipulator with two models (a) Stage moved to preparation chamber position for sample modification. (b) Stage moved to analysis chamber for XPS measurement.

The travel distance for XY axis is ±12.5 mm and for Z axis is 425 mm which is capable for both sample preparation and XPS measurements. All stages are UHV compatible and bakeable to 200^{o}C. XY tables and Z motion are driven by stepper motors for finer sample adjustment. Rotary motion is held by Al central sleeve and the bottom bearing and it has a 360^{o} rotation angle range.

2.4.2 TMD Thin Film Device Holder

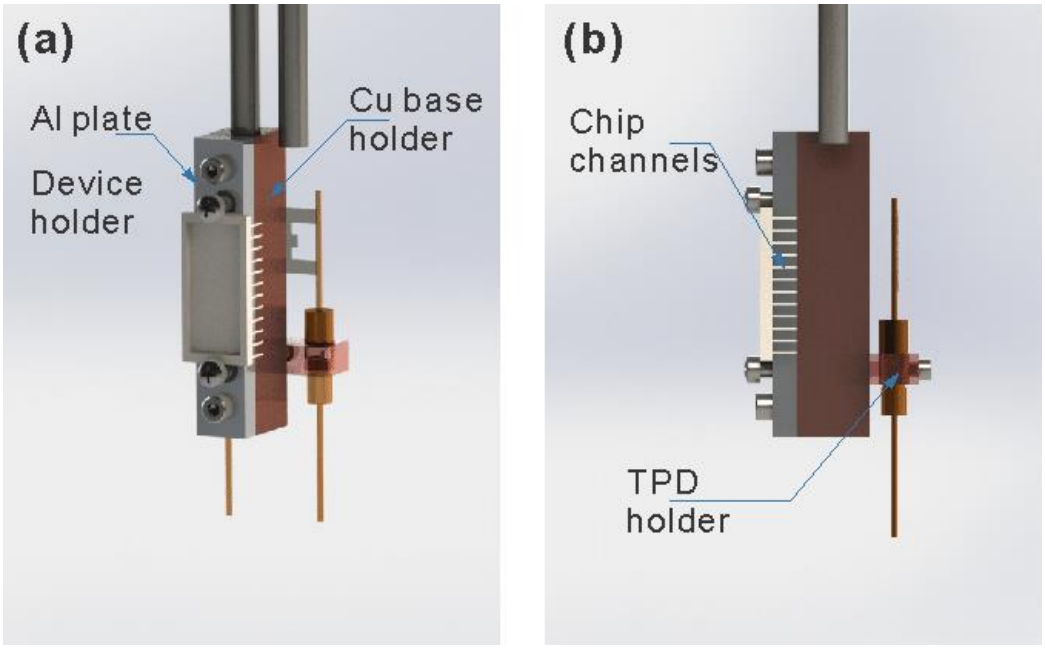

Figure 2-6: Solidworks model of thin film device holder (a), (b) Front and side views of the device holder.

The design of the device holder was focused on the I-V measurements. 24 chip channels on the ceramic chip carrier allow enough connections for the thin film devices. The Al plate stays with the chip carrier for the wire bonding. Heat transfer depends on the Cu base holder. Copper braid is employed to connect the back of the Cu base holder and the cooling line from the top of the manipulator.

2.4.3 TPD Sample Holder

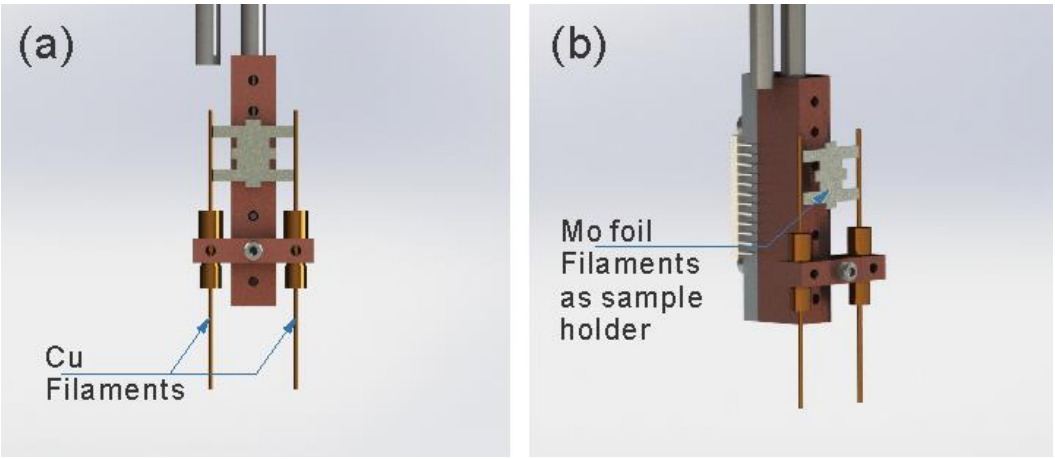

Figure 2-7: (a), (b) Solidworks model of sample holder for temperature programmed desorption.

The TPD sample holder is for the TPD spectrum measurement. TPD observes the mass of desorbed molecules. It shows what molecules are adsorbed on the surface. TPD also recognizes the different adsorption conditions of the same molecule from the differences between the desorption temperatures of molecules desorbing different sites at the surface[10]. To measure TDP, the mass spectrometer approach to the sample surface, by using the Cu filaments on the holder and Mo foil filaments, the amount of adsorbed molecules is measured by increasing the temperature at a heating rate of about 2 K/s. Several masses are simultaneously measured by the mass spectrometer, and the intensity of each mass as a function of temperature is obtained as a TPD spectrum.

Chapter 3 Controlled Argon Beam-induced Desulfurization of Monolayer Molybdenum Disulfide

The following is taken from an article I published in Journal of Physics: Condensed Matter: Ma Q., Odenthal, P., Mann, J., Le, D., Wang, C., Zhu, Y., Chen, T., Sun, D., Yamaguchi, K., Tran, T., Wurch, MeKinley, J., Wyrick, J., M., Magnone, K., Heinz, T., Rahman, T., Kawakami, R. and Bartels, L.. Controlled argon beam-induced desulfurization of monolayer molybdenum disulfide, Journal of Physics: Condensed Matter 25 252201 (2013). This was collaborative work reporting on measurements by myself and other graduate students (Odenthal, P., Mann, J., Le, D., Wang, C., Zhu, Y., Chen, T., Sun, D., Yamaguchi, K., Tran, T., Wurch, MeKinley, J., Wyrick, J., M., Magnone, K.,) on the photoluminescence/XPS system I built. Odenthal, P. from Kawakami's lab helped me to setup the photoluminescence system as well as many details experimental designs.

3.1 Overview

In this chapter, I will discuss a special Ar^+ sputtering technique that can transform single-layer MoS_2 all the way to $MoS_{1.5}$, while in situ XPS measurement reveals substantially unchanged Mo 3d states. In situ monitoring of the PL can gauge the impact of the sputter-induced defects/vacancies on the exciton dynamics; in the temperature regime between 175 and 300 K we find a decay of PL yield that decreases at ~7.0 +/-0.5 times the rate of sulfur removal.

3.2 Ar^+ Beam Sputtering

Our measurements were performed on films and isolated islands of single-layer MoS_2 grown on a SiO_2 substrate from MoO_3 and elemental sulfur, as described elsewhere [11]. Fig. 3-1 (a) shows an optical microscopy image of a representative area of a MoS_2 film used in this study. Fig. 3-1 (b) is a schematic representation of the structure of single-layer MoS_2, which consists of hexagonal top and bottom layers of sulfur surrounding a molybdenum layer. The samples were characterized in air prior to our experiments using Raman and PL spectroscopy. The right portion of the image in Fig. 3-1 (a) shows a continuous film of monolayer thickness, while the left area consists of single-layer MoS2 islands. Both regions exhibit the same PL peak at 1.87 eV, corresponding to the direct band gap. Raman spectra reveal the E12g and A1g modes, with a separation of 21 cm^{-1}, as is typically seen in single-layer MoS_2 films prepared by CVD [12, 13].

Once a sufficiently homogeneous area of the MoS_2 film exhibiting exclusively single-layer Raman and PL characteristics had been identified, the sample was attached to a temperature-controlled manipulator in an ultra-high vacuum system. For subsequent studies of sputtering, the system was evacuated and baked to reach a base pressure of $1x10^{-9}$ Torr. A Varian sputter gun operated at 500 V acceleration potential, 20 mA emission current, and 5×10^{-6}–2×10^{-5} Torr partial pressure of Ar was used for generating Ar ions. The sputter beam had a

diameter of 0.5 cm. For reference, we measured the sputter current induced by this beam on a copper surface as 0.6 and 2.2 μA, respectively, for the Ar pressures given above. In the following, this value is as an approximation of the beam current.

The XPS measurements were performed using excitation by Al Kα radiation with the emitted electrons detected by a Scienta R300 hemispheric analyzer equipped with a 2D detector. The PL experiments employed a Spectra Physics Millennia laser operating at a wavelength of 532 nm, a spectrometer with 1200 lines mm-1 grating blazed at 750 nm, and a liquid-nitrogen cooled Princeton Instruments SPEC-10 CCD detector. For in situ measurements a 50 mm focal length lens inside our UHV system was used to focus ~100 mW of pump beam onto the sample surface with a spot of ~100 μm. This results in an intensity of approximately 10 μW μm^{-2}, similar to that of typical microscope-based Raman measurements [14]. We collected the resultant PL signal in the back-scattered direction using a dichroic mirror to separate the excitation beam from PL signal.

Vacancy formation energy and thermal stability of the sputtered film was evaluated using the Vienna ab initio simulation package (VASP) [15, 16] to perform density functional theory (DFT) simulations. We employed projectoraugmented wave (PAW) [17, 18] and plane-wave basis set methods. We used the Perdew–Burke–Ernzerhof of functional (PBE) [18] to describe exchange correlation interactions and adopted a cut-off for plane- wave expansion at 500 eV. The conjugate-gradient algorithm [17] was employed for structural relaxation and

to optimize lateral atomic coordinates by minimizing the in-plane components of the stress tensor; relaxation was allowed with periodic boundary conditions until all components of the force reached a value below 0.01 eV $Å^{-1}$. Given the large number of atoms in the computational supercell (up to 192), we found sampling of the Brillouin zone with one k-point to be adequate for evaluation of the total energy. Ab initio molecular dynamic (MD) simulations utilized the Nosé algorithm [19] for setting the system temperature and a 3 fs time step. To minimize the computational cost, the cut-off for plan-wave expansion was reduced to 300 eV and the simulations ran for a total time of 12 ps.

Our measurements involved cycles of sputtering at room temperature, in situ acquisition of XPS spectra of the Mo 3d, the S 2p, and the Si 2s levels, as well as in situ PL measurement at variable temperature. To avoid sample degradation, all experiments were conducted in immediate succession to one another, with the sample maintained in ultra-high vacuum. Fig. 3-2 (a)–(c) displays the evolution of XPS spectra during sputtering at 2 $x10^{-5}$ Torr Ar pressure, corresponding to a net sputter current of 2.2 μA. Fig. 3-2 (a) shows representative spectra of the Mo 3d 3/2 and 5/2 peaks for increasing sputter times. The sulfur 2s peak is also visible on the low-energy side of the Mo-derived features. We observe no appreciable reduction in Mo 3d intensity. Further, the shape of the Mo 3d 3/2 and 5/2 doublet remains essentially unchanged, as is best seen in the energy-aligned superposition below the individual spectra in Fig. 3-2 (a) and (b). In order to account for potential charging of the MoS_2 sample on the thick oxide layer, we treat the Si 2p peak (Fig.

3-2(c)) as a standard and reference all other states to it. Fig. 3-2(d) shows the evolution of the Mo 3d intensity as a function of sputter time.

3.3 Results and Discussion

The sulfur signal (Fig. 3-2(b)), in contrast to the Mo 3d feature, exhibits a significant reduction in strength from sputtering, with little change of the overall peak shape. Fig. 3-2(d) shows that the total sulfur content, normalized to 2 for the unsputtered film to account for the different XPS yields of the Mo and S states, decreases with sputter time. Within the duration of this experiment, we observe a reduction of the sulfur content of the film by 25%, or 50% of the top sulfur layer in the MoS_2 structure (Fig. 3-1(b)). This corresponds to an average sputter yield of 0.03 per Ar^+ ion. A first-order approximation of the sulfur signal decay (red line in Fig. 3-2(d)) corresponds to an exponential fit with a rate constant of 1.6×10^{-3} 1 s^{-1} or 1.4×10^{-4} cm^2 C^{-1}.

We ascribe the selectivity to sulfur removal to the close mass match between the Ar^+ ions and the sulfur atoms, as well as to the low Ar^+ energy; 3 keV Ar^+ ions are incapable of removing Mo completely from our substrates. The silicon peak (Fig. 3-2(c)) serves as an internal reference and is not significantly affected by sputtering or exposure to air.

Apart from a shift to lower binding energy, likely arising from charging of the sputtered MoS_2 film with respect to the underlying SiO_2 layer, we observe little change of the peak shape of the Mo- and S-derived features (lower part of Figs. 3-

2(a) and (b)). The latter suggests that despite sputtering, the MoS_2 film retains its homogeneity and its overall MoS_2 structure; we speculate that this is achieved by the presence of an unperturbed bottom sulfur layer that retains the structure of the Mo layer rigid, despite the absence of some of the top-layer sulfur atoms. We further support this argument in the following paragraphs.

Prior to processing, the sulfur and the molybdenum coverage of the samples correlate with one another. There is neither a significant quantity of sulfur in the absence of molybdenum nor is there appreciable incorporation of sulfur into the substrate surface during preparation. We reach these conclusions by aligning the sample so that the spatially resolved axis of our 2D detector lies along the horizontal of Fig. 3-1(a), i.e., by detecting the XPS yield from sample areas covered by a thick MoS_2 film on one side (where we find strong signal both for S and Mo), across an area with MoS_2 islands (where we find reduced signals for both S and Mo), and ending at a sample area devoid of MoS_2 features on the other side (where we find neither significant Mo nor S signal). This observation indicates that the S/Mo ratio that we track in the XPS-sputter cycles can indeed be related to modification of the MoS_2 monolayer and is not significantly affected by any other possible sulfur source in the surface region. The fact that the MoS_2 film is the material being modified is further buttressed by the film's dramatic change in stability after processing. XPS measurement on a sputtered film after exposure to air exhibit significantly broadening Mo 3d 3/2 and 5/2 peaks, as well as S 2p peaks (bottom of Fig. 3-2(a) and (b)). We attribute this to extensive oxidation.

After sputtering and air exposure, atomic force microscopy reveals degradation in film smoothness, and the film's Raman response is significantly reduced. On the other hand, the original, unprocessed films are found to be stable in air.

To confirm that a MoS_2 film with a significant fraction of its top sulfur atoms removed is structurally stable in vacuum for the temperature range of our measurements (≤350 K), we performed DFT calculations on (6x6) and (8x8) MoS2 units supercells from which we removed a hexagon of 7 adjacent top-layer sulfur atoms (Fig. 3-1(d)). Such an arrangement allows us to examine the effect of creation of a relatively large vacancy cluster on the stability of the single-layer MoS_2. Structural relaxation maintains the overall shape of the film and changes the original Mo–Mo bond length inside the S-depleted region ≤5%. Allowing the film to evolve at 350 K over a 12 ps interval within *ab initio* MD leads to no structural change of the film, further supporting the stability of such a sulfur-depleted structure. We note that our calculations do not account for the support of the film structure through an underlying substrate and assume a comparatively large region of depletion of the surface sulfur. Both of these effects generate higher strain than is likely present in the films under experimental conditions.

To explore the impact of sputtering on the optical response of our films, we performed *in situ* PL measurements. Fig. 3-3(a) and (b) show PL spectra acquired at temperatures of 175 and 300 K. In both cases, we observe a clear PL signal prior to sputtering, which decays with sputter exposure. The inset of Fig. 3-3(a) and (b) shows the Mo 3d XPS spectra acquired at 300 K at each of the sputter

times, which are virtually unchanged throughout the experiment. By comparison of their intensity to the sulfur XPS intensity (not shown), we obtain the amount of sulfur removed. In addition, we observe a well- known reduction of PL yield with increasing temperature [20].

We fitted each PL peak with a Gaussian curve and a constant background. Fig. 3-3(c) shows the evolution of the Gaussian amplitude with sputter time. For purposes of comparison, we plot the relative evolution of the PL yield for each temperature as a function of the reduction in sulfur content of the film (Fig. 3-3(c)).

The PL yield decreases as sulfur is removed. For 10% of sulfur depletion, the PL yield is reduced by almost 80%, i.e., an average decrease of ~(7.0 +/- 0.5) times the rate of decrease of the sulfur concentration. Note that in Fig. 3-2 and in our discussion the fraction of sulfur is referred to the overall sulfur content of the MoS_2 monolayer structure. As sputtering is far more likely to remove sulfur in the top layer than in the bottom sulfur layer, the percentage values are twice as high if referred only to the top sulfur layer. As seen in Fig. 3-3(c), the quenching behavior of the PL is largely unchanged over the temperature regime addressed in this study.

The exciton dynamics underlying the quenching of the PL by sputtering is likely complicated. A rigorous treatment has to account for changes to the MoS_2 band structure, absorbance, and charging, which is beyond the scope of this study. However, we note that good agreement with the data can be achieved if one

assumes (a) that the MoS_2 single- layer absorbance is not significantly changed by sputtering, (b) that quenching occurs whenever a photon is absorbed in a MoS_2 unit cell that is perturbed, i.e., missing its top sulfur atom or missing lateral coordination due to a sulfur atom being removed from a directly adjacent unit cell, and (c) that in all other cases the PL yield is identical to the that of the unperturbed system. To obtain values for the PL quenching from these assumptions we have performed a simple simulation (dotted line in Fig. 3-3(c)). Using a MoS_2 film of 200 x 200 unit cells, we randomly remove a varying fraction of the top- layer sulfur atoms and evaluate for 1000 arbitrarily chosen locations whether or not the unit cell is perturbed (as defined above). While this model provides agreement with the experiment, we note that a combination of less than unity quenching efficiency of defects and longer exciton diffusion lengths would yield similar overall behavior [13].

In summary, we have shown that sputtering with a beam of low-energy argon ions provides a method for selective desulfurization of monolayer MoS_2. The spectroscopic studies and DFT modeling suggest that the basic physical structure of the MoS_2 remains largely intact as the sulfur is removed. Our findings suggest that low-energy argon sputtering may have significant potential for the activation, functionalization, and modification of MoS_2 layers. Although not studied systematically, the sharp increase in reactivity of the processed MoS_2 monolayer is apparent from its rapid oxidation in air.

3.4 Figure

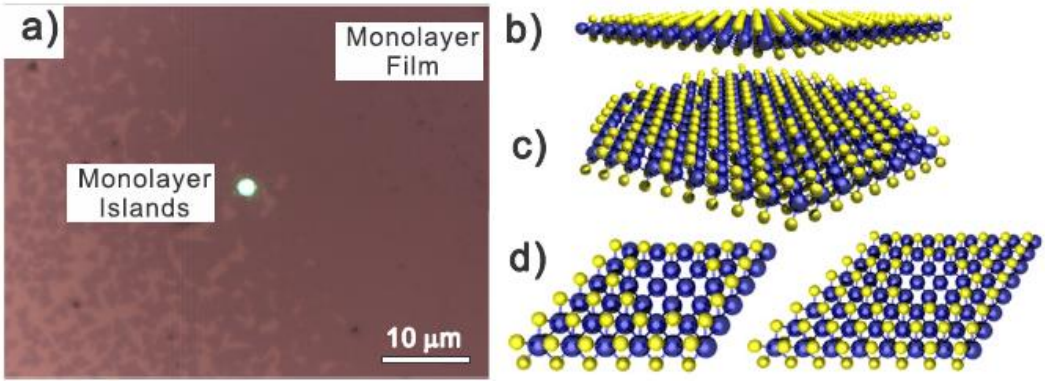

Figure 3-1: (a) Optical micrograph of the type of MoS_2 films used in this study, with single-layer islands on the left and a continuous single-layer film on the right of the imaged area. The laser spot is 2 µm in size and was used for measurement of Raman spectra in air. (b) The structure of an ideal MoS_2 monolayer film, consisting of a plane of Mo atoms surrounded by two planes of S atoms. (c) A representation of a possible structure of the film after sputter removal of 12.5% of its sulfur (25% of the top-layer sulfur atoms). (d) A compact 7-atom top-layer sulfur vacancy in the two computational supercells used in this work. These structures were found to be stable within our ab initio molecular dynamics simulation at 350 K.

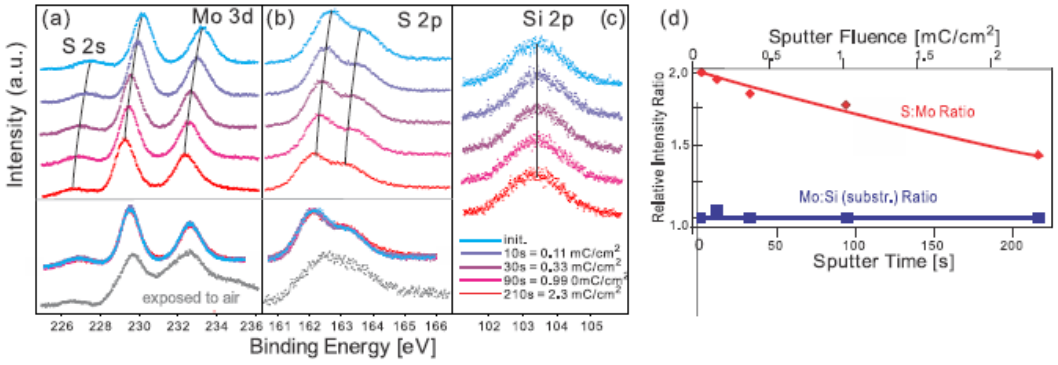

Figure 3-2: XPS spectra of (a) the Mo 3d 3=2 and 5=2 states, as well as the S 2s (weak features on the left), (b) the S 2p state, and (c) the Si 2p state. The spectra (from the top to the bottom) were acquired after increasing amounts of sputtering. To account for surface charging, the spectra at different sputter times were aligned so that the Si 2s peak remains at constant energy. The lower parts of (a) and (b) show spectra scaled and shifted for the best overlay of the peak shape, as well as the corresponding spectra after exposure to air. (d) The evolution during sputtering of the intensity of the Mo XPS signal referenced to the substrate Si peak and normalized to unity, and the S:Mo XPS ratio normalized to 2. While the Mo content is seen to remain essentially constant, the amount of sulfur decreases significantly during sputtering.

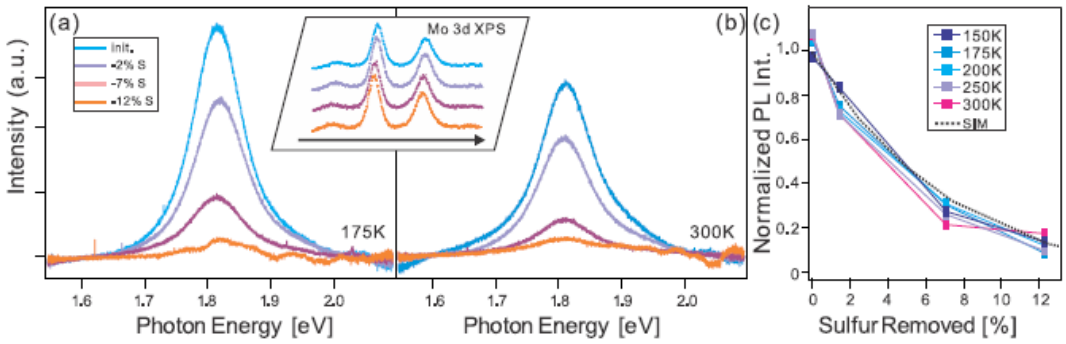

Figure 3-3: PL spectra of a MoS_2 sample for increasing sputter time/sulfur depletion recorded at temperatures of (a) 175 K and (b) 300 K. The inset shows the corresponding Mo 3d 3/2 and 5/2 XPS spectra, which remain virtually unchanged. At higher temperatures, a lower initial PL yield is observed; during sputter removal of sulfur the PL yield decreases at both temperatures. (c) The normalized intensity of the PL signal as a function of the percentage of total sulfur removed for different indicated temperatures. The dotted line (sim) corresponds to the model described in the text.

Chapter 4 Post-growth Tuning of the Bandgap of Single-layer Molybdenum Disulfide Films by Sulfur/Selenium Exchange

The following is taken from an article I published in ACS Nano: Ma Q., Isarraraz M., Wang C., Preciado E., Klee V., Bobek S., Yamaguchi K., Li E., Odenthal, P., Nguyen A., Barroso D., Sun D., Palacio G., Gomez M., Nguyen A., Le D., Pawin G., Mann, J., Heinz, T., Rahman, T., and Bartels, L., Post-growth tuning of the bandgap of single-layer Molybdenum disulfide films by sulfur/selenium exchange, ACS Nano, 8 (5), pp 4672-4677 (2014). This was collaborative work reporting on measurements by myself and other graduate student (Isarraraz M., Wang C., Preciado E., Klee V., Bobek S., Yamaguchi K., Li E., Odenthal, P., Nguyen A., Barroso D., Sun D., Palacio G., Gomez M., Nguyen A., Le D., Pawin G., Mann, J., Heinz, T., Rahman, T., and Bartels, L.) members of the Bartels group on the XPS system I built. Computational support came from D. Le of the group of T.S. Rahman of the University of Central Florida.

4.1 Overview

A major opportunity for 2D materials and their applications lies in the tunability of bandgaps and the preparation of heterojunctions from materials with different gaps.[21-23] In this chapter, we demonstrate the manipulation of the bandgap of single-layer MoS_2 with a simple sputtering-based procedure. This

approach is compatible with lateral patterning of 2D layers and should permit the formation of in-plane heterojunctions at defined locations. We first characterize the substitution process by examining the removal and subsequent reinsertion of sulfur atoms. We find only a modest net decrease of the photoluminescence efficiency of the material, which is often used as an indicator of its quality.[24-26] We then present results for the insertion of selenium atoms after sputtering and use of a different organic precursor. This procedure is found to reach an apparent limit when approximately half of the top-plane sulfur atoms are replaced by selenium atoms.

4.2 Materials and Methods

We utilize MoS_2 single-layer films CVD-grown on SiO_2/Si substrates by the method described in previous publications. [27],[28] All experiments proceed in an ultrahigh vacuum (UHV) chamber with a base pressure of $5x10^{-10}$ torr and equipped with an ion sputter gun (Varian), an hemispherical electron energy analyzer (Scientia VG R3000), and a Mg X-ray source for X-ray photoelectron spectroscopy (XPS). The XPS analyzer collects electrons from a 0.6 mm x 4 mm area on the sample. The apparatus permits *in-situ* photoluminescence (PL) spectroscopy from the sample within the UHV chamber. This is accomplished using an external 532-nm solid-state laser for excitation, a 50-mm lens within the chamber for focusing the laser excitation and collecting the photoluminescence, and a spectrometer (Verity SD 1024) with a cooled CCD array for PL detection. The laser power on the sample was ~50 mW, focused to a spot diameter of ~100 μm. Details of

computational methods are described in the supporting materials section.

Removal of sulfur atoms proceeds via exposure of the sample to a 500 V Ar^+-beam, as described in Ref. [5]. Each sputter cycle takes 4 ±1 s. We use a beam current of 0.6 μA, with a separation between ion gun and sample of 16 cm. Immediately following sulfur removal, we expose the sample to 3L of either benzenethiol (BT) or diseleno-diphenyl (DS) (both from Aldrich) through a leak valve and through evaporation from a glass capillary, respectively. We then anneal the sample to ~600K for 10 min. We perform PL and XPS measurements after cool-down.

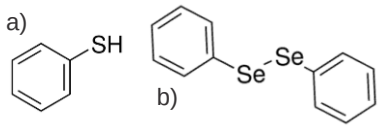

Scheme 1: (a) benzenethiol (BT); (b) diselenodiphenyl (DS)

4.3 Results and Discussion

Before discussing insertion of Se into a single-layer MoS_2 film, we characterize the method for the reinsertion of sulfur atoms. Fig. 1a) shows the PL intensity of an as-prepared (red) single-layer MoS_2 film as a function of temperature, revealing a well-studied decrease in PL yield with increasing temperature.[20, 25, 29, 30] Adsorption of 3ML of BT, an organic sulfur source, at 150K reduces the MoS_2 PL yield. Upon heating the sample above ~180K, BT is desorbed intact, as verified by mass spectrometry. We find that strength and the spectral position of the PL then return to the values found for bare MoS_2 (Fig. 4-1a

and inset). The recovery of the PL properties of the MoS_2 single-layer film after BT desorption indicates stability of the MoS_2 film (prior to activation by sputtering) to exposure to the chalcogen source.

Activation of the MoS_2 film through sputtering reduces its PL yield significantly as a consequence of increased non-radiative exciton recombination at defect sites.[5] This behavior is apparent by comparison of the red and blue lines in Fig. 4-1b. Annealing the film to 600K (green line) results in partial recovery of the PL yield, presumably through local healing of film defects. Subsequent exposure of the activated film to BT at room temperature, followed by annealing to 600K, fully restores the room-temperature PL intensity. The film extracts sulfur from the BT precursor, through a process analogous to the use of MoS_2 as a hydrodesulfurization catalyst.[31] While the recovery at room temperature very nearly reaches the original level, at lower temperatures, a modest reduction in the overall PL yield is still present, which we attribute to longer exciton lifetimes allowing them to diffuse more readily to defect sites.[30] This effect can be reduced by avoiding the annealing step (green line) between sputtering of the film and the chalcogen exposure. We anticipate that optimization of the process parameters (amount of sulfur removed, BT exposure, annealing temperature, etc.) will further improve the film quality. The sputtered films show a slight blue shift of the PL spectrum (see inset of Fig. 4-1), which disappears after sulfur reinsertion.

If we use DS (the organic selenium precursor) instead of BT, the behavior is fundamentally different: while we still observe significant recovery of the PL yield after exposure and annealing, the spectral position of the PL shifts to longer wavelengths, as expected for the insertion of Se into the film. Fig. 4-2 shows PL spectra acquired on a single-layer MoS_2 film as a function of the number of DS insertion cycles. Initially, we find the typical emission of MoS_2 at 670 nm. With increasing number of insertion cycles, the PL feature shifts continuously to longer wavelengths. The PL emission spectrum remains a single, well-defined peak, consistent with recent findings for $MoS_{2(1-x)}Se_{2x}$ single-layer alloy films and indicating the formation of a relatively homogeneous film.

Fig. 4-3 summarizes an experiment in which we highlight the ability to recover the PL intensity by reinsertion of Se atoms. We first treat the sample by sputtering for three cycles, each sputtering process reducing the film's PL yield (Fig. 3a, blue line). Based on the data of Ref. [5], this suggests the removal of almost 10% of the sulfur atoms. Exposure to DS after the third cycle partially restores the film's PL yield (red line). Subsequent cycles of sputtering and DS insertion further increase the PL to approximately 90% of the original intensity. We attribute the residual decrease in PL to a combination of a slightly lower PL yield in $MoS_{2(1-x)}Se_{2x}$ as compared to MoS_2 and sputter damage that is not completely healed during the Se insertion cycles. If we perform only a single sputter cycle prior to the first selenium insertion step, as was done for the measurements presented in Figs. 4-2 and 4-4, this effect is less pronounced.

The spectral shift of the PL decreases in successive cycles of sputtering and Se insertion. This behavior can be rationalized by the decreasing fraction of S atoms exposed in the MoS_2 film in successive cycles; we discuss this effect below in detail. The final PL spectral shift varies in the range between 20 and 30 nm from sample to sample. The terminal red shift of the sample of Fig. 4-3 of 27 nm corresponds to a bandgap shift of 0.07 eV, almost one quarter of the difference between the MoS_2 and $MoSe_2$ bandgaps. Previous work on $MoS_{2(1-x)}Se_{2x}$ films revealed a nearly linear dependence of the PL emission energy on Se content. Based on this calibration, the PL shift corresponds to replacement of 21% of the total sulfur content of MoS_2 by selenium atoms. Once this point is reached, subsequent sputter-insertion cycles do not appreciably shift the PL position, but produce a slight deterioration of the overall PL yield, presumably reflecting sputter defects that are not fully annealed.

We use *in-situ* XPS to confirm the insertion of selenium into our films. Fig. 4 shows a sequence of spectra of the pertinent core-level peaks for the sample of Fig. 4-2. With the exception of the rise of the Se 3d peak and reduction of the S 2p peaks (by ~22%), we do not observe a change in the sample's features. We also monitored the area of the carbon 1s peak, but did not find any signature of this element. While the XPS results indicate a S/Se exchange consistent with the shift of the optical bandgap, these measurements may be affected by systematic errors associated with removal of excess sulfur from or attachment of excess selenium to the film or the substrate surface.

Our previous study shows that the mild sputtering process does not remove an appreciable amount of Mo from the film and that the XPS Mo electronic configuration remains unchanged, suggesting the overall structural stability of the chalcogen-depleted film in vacuum. In air, however, the sputtered films deteriorate. Ex situ PL measurements in air of the samples after Se insertion using a Raman microscope (Horiba LabRam) show rapid sample deterioration during optical excitation. We attribute this degradation to the presence of a comparatively low density of unsaturated bonds/sites from sputter damage to the film. Future work will address avenues for film passivation through in situ capping by a barrier layer.

Having demonstrated the insertion of Se into our films, we wish to discuss the observation of a terminal bandgap that falls short of the optical bandgap shift expected for complete S/Se exchange. Insertion of Se from an organic source at comparatively low annealing temperature may favor insertion into the top chalcogen plane.[27, 32] We performed density functional theory (DFT) calculations to determine the expected behavior in the limiting case of insertion of Se exclusively into the top chalcogen plane (the supporting information provides computational details). We utilize 6x6 MoX_2 supercells and compute bandgaps for different top-plane arrangements of Se and S atoms. Fig. 4-2b compares the bandgap predictions for homogeneous $MoS_{2(1-x)}Se_{2x}$ single-layer alloy films (blue, from Ref.[27]) with the behavior expected for strictly top-layer insertion (red). The bandgap for the same Se content are seen to be quite similar.

We note, however, that insertion of Se induces expansion of the equilibrium

$MoS_{2(1-x)}Se_{2x}$ lattice constant. The computed equilibrium lattice spacing for top-plane and homogeneous Se insertion do not differ meaningfully for the same total Se content and suggest a 4% increase for $MoSe_2$ compared with MoS_2, in line with literature values.[32, 33] The degree of expansion of the treated films is not known directly from experiment. The nucleation sites for film growth[34, 35] may serve as pinning centers for the film, preventing complete lateral expansion, especially for the case of the continuous films as used in this work.[28] We have accordingly analyzed the film's bandgap for different fractions of the equilibrium expansion for various Se concentrations (top four traces in Fig. 4-2b). In the absence of an expansion (brown trace), the competition between Se insertion (leading to decreased bandgap)[32, 33] and compressive strain of the film (leading to increased bandgap with small compressive strain)[36, 37] causes the bandgap to vary quite differently from the case in which strain is relaxed. For low Se concentrations, the gap widens slightly, followed by narrowing at higher Se concentrations. For partial lattice relaxation, the variation of the bandgap with the Se contents becomes smaller and at 50% relaxation the initial bandgap widening vanishes, in good agreement with our experimental results. However, even at 75% of the equilibrium expansion, we still find a marked deviation from the equilibrium case, leading to a bandgap reduction for complete S/Se exchange in the top layer that is compatible with our experimentally observed value. We conclude that partial pinning of the film on the substrate, and the associated lack of lattice relaxation, may reduce the variation of the bandgap with Se-content. This suggests that the

observed reduction in bandgap shift with increased cycle number (Fig. 4-2a) may also reflect an increase in strain in the film, rather than exclusively a reduction of the amount of inserted Se.

Thus, although both XPS and the PL suggest some 22% exchange of S by Se, the precise match of these values may reflect possible systematic error in XPS and underestimation of the Se-insertion from the PL measurements of the bandgap. We note that our computational approach with periodic supercells does not allow for bending of the film as a consequence of Se insertion. We have performed calculations of phonon dispersions (see supporting material) and find dynamic stability of the flat, free-standing film at any top-layer Se concentration. We note, however, that a combination of a bending in the film and pinning to the substrate may generate a limit to stable Se insertion short of complete S/Se exchange. These issues will be examined in future measurements starting from Se-rich material.

The simple procedure presented here to tune the bandgap of single-layer transition metal dichalcogenide films after growth suggests new research directions. Local patterning of the bandgap should be possible by control of the sputtered region of the film. This would provide a means to produce heterojunctions and spatial variation of the bandgap for other purposes. At the same time, this study shows that induced strain in the film may also play an important role, providing another route for control of the bandgap.

4.4 Methods

Initial film growth was achieved in a tube furnace at ~1000 K using SiO_2/Si substrates of ~2 cm x 2 cm in size. MoO_3 powder and liquid BT were used as metal and chalcogen sources, respectively. Our setup and method are described in detail in previous publications [38, 39].

All experiments were carried out in an ultrahigh vacuum (UHV) chamber with a base pressure of 5 x 10^{-10} Torr. This system is equipped with an ion sputter gun (Varian), a hemispherical electron energy analyzer (Scientia VG R3000), and an Mg X-ray source for X-ray photoelectron spectroscopy (XPS). The XPS analyzer collects electrons from a 0.6mm x 4mm area on the sample.

The apparatus permits PL spectroscopy from the sample within the UHV chamber. This is accomplished using an external 532 nm solid-state laser for excitation, a 50 mm lens within the chamber for focusing and collecting the photoluminescence, and a spectrometer (Verity SD 1024) with a cooled CCD array for PL detection. The laser power on the sample was ~20 mW, focused to a spot diameter of ~100 μm.

Each sputter cycle takes 4 ± 1 s and is performed with the sample held at room temperature. We use a beam current of 0.6 μA, with a separation between ion gun and sample of ~16 cm. We anneal the sample to ~600 K by means of indirect heating for 10 min. The temperature is measured on the sample holder. We perform PL and XPS measurements after cool-down.

AFM measurements utilize a Dimension 3100 Nanoman by Veeco using

silicon coated tips by Bruker. AFM images reveal features of angstrom-scale height on the SiO_2 substrate, but the MoS_2 films appear smooth both before and after the procedure described in this manuscript.

4.5 Figure

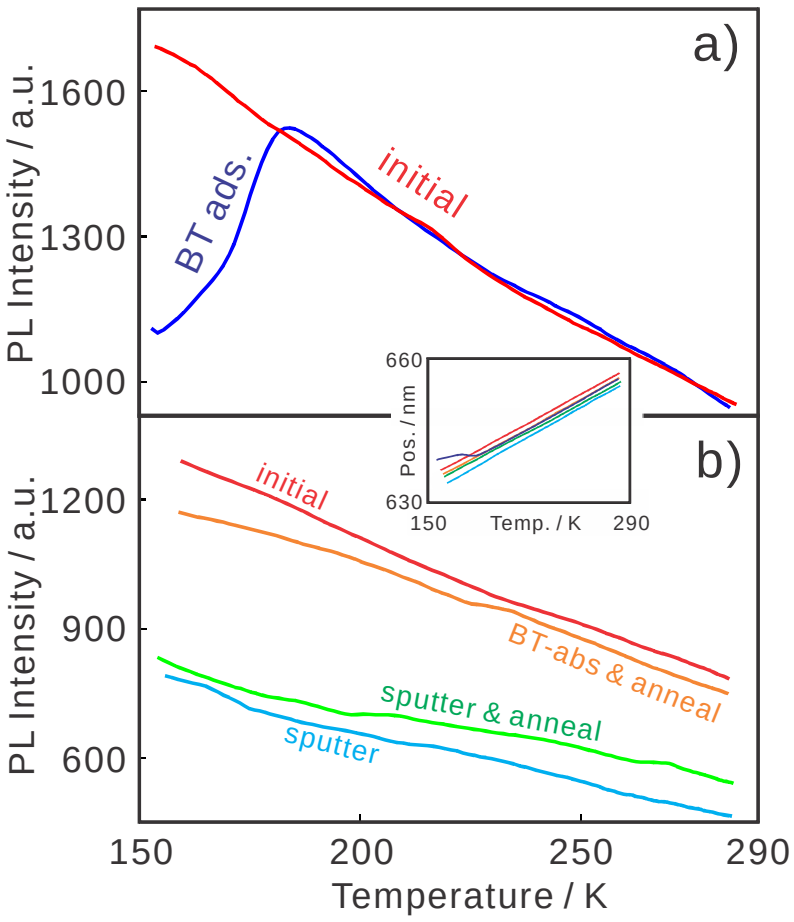

Figure 4-1: (a) PL intensity of an as-prepared (red) MoS_2 film and after 3L BT-exposure at 150K as a function of substrate temperature. Upon BT desorption at ~180 K (as verified by mass spectrometry), the PL intensity and PL position (inset) recover their original values. (b) PL of the MoS_2 single-layer film prior to (red) and after (blue) sputtering. Data are also shown after a subsequent annealing to 600K (green), followed by BT absorption and a further annealing cycle (orange). The PL intensity and spectral position (inset) essentially recover their original values.

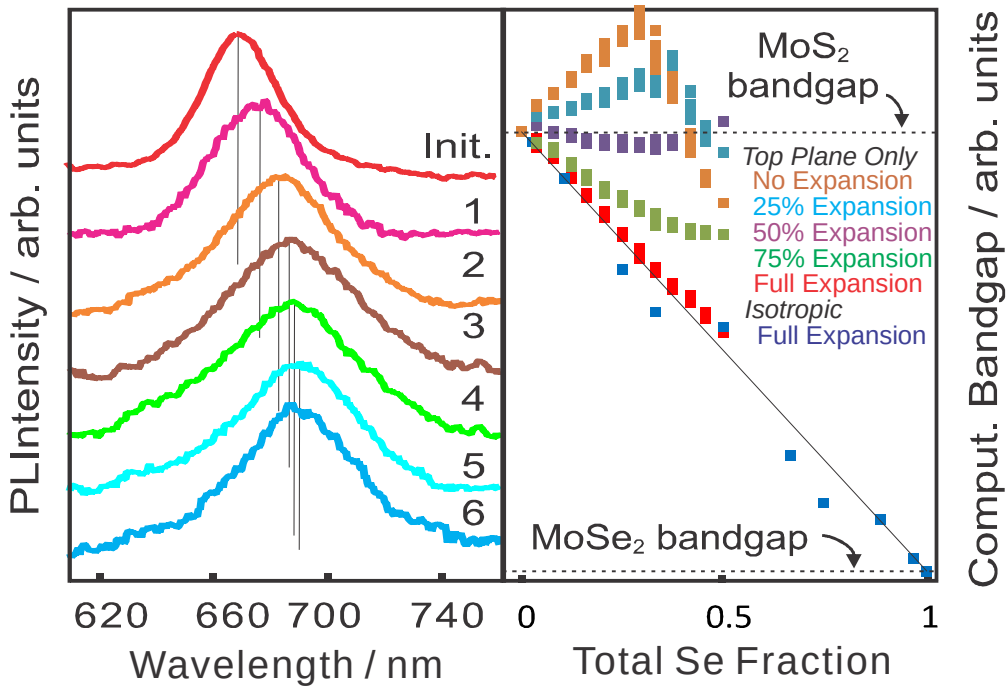

Figure 4-2: a) Normalized room-temperature PL spectra of a single-layer MoS_2 film after sputtering and DS insertion cycles. The PL peak red shifts and broadens until saturation is reached. The vertical lines indicate the peak position as a guide to the eye. b) DFT-based bandgap of $MoS_{2(1-x)}Se_{2x}$ between the limits of pure MoS_2 and pure $MoSe_2$ for homogeneous $MoS_{2(1-x)}Se_{2x}$ (blue, from Ref. [27]) and for insertion of Se exclusively into the top chalcogen plane (red). Insertion of Se causes lateral expansion of the film lattice ($MoSe_2$ has a lattice constant ~ 4% larger than MoS_2). Restriction of lattice expansion to a certain percentage of the equilibrium value for any Se concentration results in the bandgap values shown in green, pale blue, purple and brown. The height of the data points indicates the spread of values for different arrangements of the Se atoms in the computational supercell.

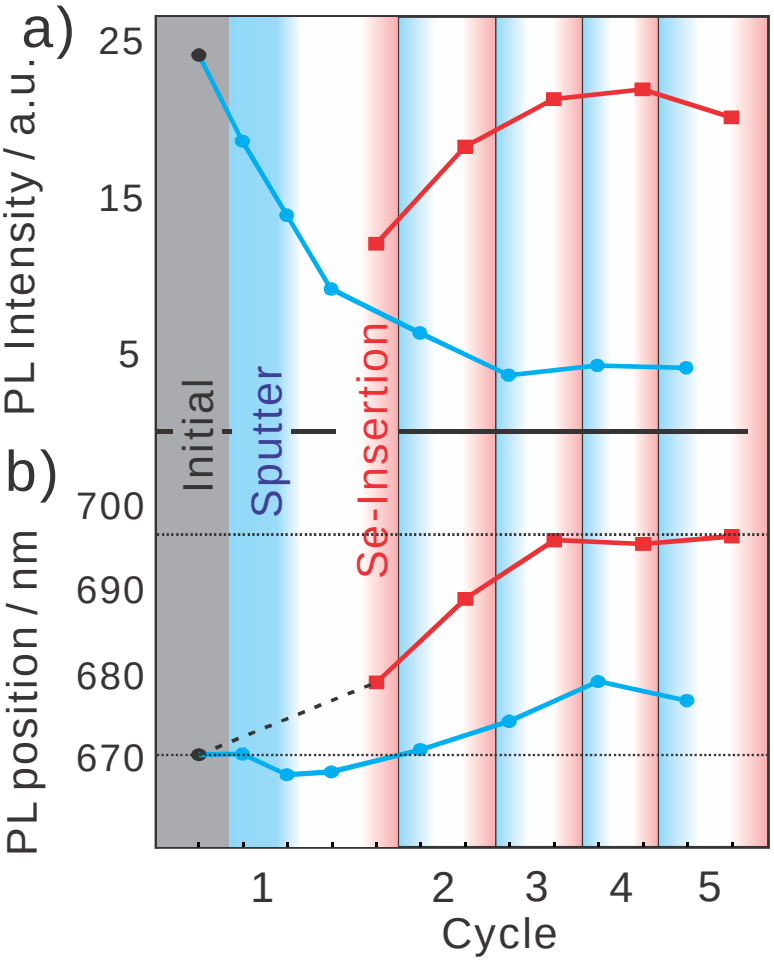

Figure 4-3: Room-temperature PL intensities and peak positions of a MoS_2 single-layer film after cycles of sputtering and DS exposure. Top: repeated sputtering reduces the initial PL intensity (blue). When DS insertion steps are interspersed with sputtering cycles, the film's PL yield nearly recovers to its initial value. Bottom: sputtering blue shifts the PL peak position; insertion of Se causes a red shift that saturates after approximately the third insertion cycle. The peak position shifts by a total of 27 nm or 71 meV.

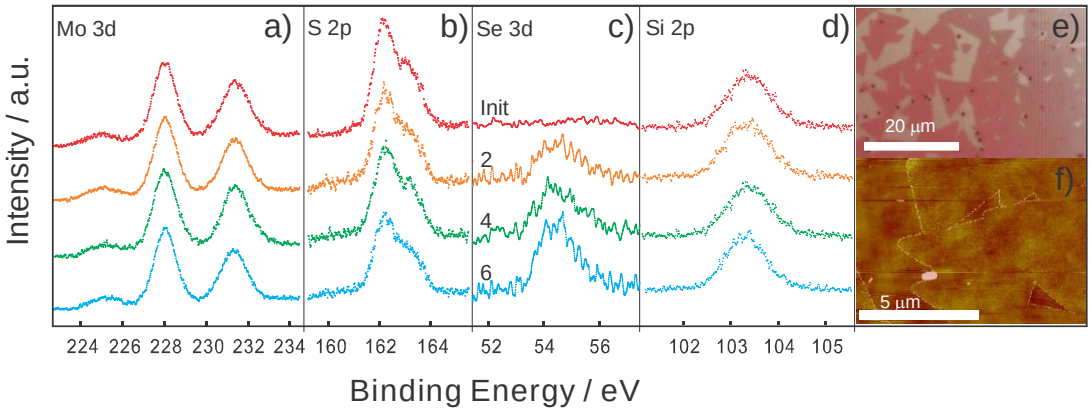

Figure 4-4: *in-situ* XPS spectra of the sample of Fig. 2 after 0, 2, 4, 6 cycles of selenium insertion. a-d) show the Mo 3d, S 2p, Se 3d, and Si 2p substrate peaks, respectively. Initially no selenium is signature is found. Its presence is visible after 2 cycles and increases with the number of cycles, with a concomitant decrease in the sulfur signal. e,f) optical and AFM microscopy in air of the edge of the MoS_2 film after 6 selenium insertion cycles. The flat and smooth triangular islands and regions of continuous film are indistinguishable from images of the untreated film.

Chapter 5 2-Dimensional Transition Metal Dichalcogenides with Tunable Direct Band Gaps: $MoS_{2(1-x)}Se_{2x}$ Monolayers

The following is taken from an article I published in Advanced Materials: J. Mann, Q. Ma, P. Odenthal, M. Isarraraz, D. Le, E. Preciado, D. Barroso, K. Yamaguchi, G. Palacio, A. Nguyen, T. Tran, M. Wurch, A. Nguyen, V. Klee, S. Bobek, D. Sun, T. Heinz, T. Rahman, R. Kawakami and L. Bartels., 2-Dimensional Transition Metal Dichalcogenides with Tunable Direct Band Gaps: $MoS_{2(1–x)}Se_{2x}$ Monolayers, Advanced Materials 10.1002/adma.201304389 (2013). This was collaborative work reporting on measurements by myself and other graduate student (Isarraraz M., Wang C., Preciado E., Klee V., Bobek S., Yamaguchi K., Li E., Odenthal, P., Nguyen A., Barroso D., Sun D., Palacio G., Gomez M., Nguyen A., Le D., Pawin G., Mann, J., Heinz, T., Rahman, T., and Bartels, L.) members of the Bartels group on the XPS system I built. Computational support came from D. Le of the group of T.S. Rahman of the University of Central Florida.

5.1 Overview

In this chapter, we present a simple synthetic route to produce single-layer $MoS_{2(1-x)}Se_{2x}$ alloy films with an arbitrary S/Se ratio. This allows us to tune the direct optical gap continuously between the values of single-layer MoS_2 (1.87 eV) and $MoSe_2$ (1.55 eV) and to create thereby the building blocks for band-gap engineered 2D structures.

5.2 Materials and Methods

With the intense recent interest in atomically thin MoS_2 materials, several methods have been developed to prepare films that complement the exfoliation of bulk crystals. These approaches include CVD using $MoCl_5$ or MoO_3 and S as sources,[40-43] laser-based thinning,[44] plasma thinning,[45] liquid exfoliation,[25, 46-48] graphene assisted growth,[49] and the sulfurization of molybdenum films prepared by e-beam deposition[12] or dip coating.[50] Thicker films of MoS_2 and $MoSe_2$[51] have been grown by numerous CVD techniques. For growth of monolayers of MoS_2, the methods typically lead to single-layer triangular or hexagonal islands several microns in size, as well as to elongated areas of single-layer film 100 microns in length.

In order to be able to insert selenium into the growth process, instead of elemental sulfur we use thiophenol (Aldrich: 240249) dissolved in tetrahydrofuran as sulfur source, to which diphenyl-diselenide (Aldrich: 180629) is added to adjust the sulfur/selenium ratio. We place the growth substrate, typically a Si(110) wafer covered by a 300-nm SiO_2 layer, in the center of a tube furnace. The substrate is located either directly on top of a boat carrying MoO_3 powder or, in order to achieve more homogeneous growth, it is supported by a Mo-mesh (Alfa: 40908) above a flat Mo shim covered by MoO_3 powder. Growth is achieved by injecting the liquid chalcogen source (~ 1ml) via a long syringe needle near the process region of the tube furnace at 650-700° C (Fig. 1a shows a sketch and the supporting material shows a photograph of the setup) immediately afterwards the furnace heating is switched off. Growth has been achieved over a temperature range of 50° C using both tube furnaces with 1” and 2”

process tubes. Both the oxygenate solvents and post-growth (after the furnace has cooled to 500° C) application of H_2 gas are necessary to avoid formation of a carbonaceous deposit on the metal dichalcogenide monolayer, which quenches the film's photoluminescence (PL) (although Raman spectroscopy indicates that a monolayer film has formed). Fig. 1 b, c show photographs of the size of substrates we typically use.

Sulfur-rich TMDs grow into single-layer films of larger lateral extent than selenium-rich ones, with pure $MoSe_2$ resulting into the smallest single-layer film areas. The growth process favors sulfur incorporation; thus, the Se:S ratio in the source solution needs to exceed that of the desired film composition: for instance, our $MoS_{1.68}Se_{0.32}$ sample (*vide infra*) was grown using a Se:S mole fraction of 1:0.7.

5.3 Results and Discussion

Fig. 5-1 d,e shows optical and atomic force microscopy images of the resultant films, which resemble those found in prior CVD growth of MoS_2.[40-43, 52] Because of the growth on an insulating substrates and our lack of a selenium-compatible transfer method, no electron microscopy is available.

Fig. 5-2a shows room-temperature (RT) PL spectra for a series of $MoS_{2(1-x)}Se_{2x}$ films of different composition. These measurements use a laser operating at a wavelength of 532 nm (Coherent Verdi), a spectrometer with 1200 lines/mm grating blazed, and a liquid-nitrogen cooled Princeton Instruments SPEC-10 CCD detector.

The samples range from pure MoS_2, with a PL emission peak at 1.87 eV, to

pure $MoSe_2$, with a PL peak at 1.54 eV. The spectra reveal reasonably sharp and bright PL features. We only evaluated sample areas that show strong PL indicative of monolayer film. Images can be found in the supporting material. We obtain the chemical composition of the samples from the relative intensity of the S 2p and Se 3p features measured using X-ray photoelectron spectroscopy (XPS). The XPS measurements are performed using excitation by Al-K_α radiation, with the emitted electrons analyzed by a hemispheric analyzer (Scienta R300), which has a spatial acceptance of 0.7 mm × 0.5 mm. Because of uncertainty in the alignment of the XPS spot with the center of the homogeneous area, we estimate an uncertainty of $\Delta x = \pm 0.1$ in the inferred composition of the $MoS_{2(1-x)}Se_{2x}$ alloy.

The variation of the optical gap with the composition of the $MoS_{2(x-1)}Se_{2x}$ alloy monolayers is presented in Fig 5-1b. The results are based on the A exciton emission energy in PL spectra like those in Fig. 5-2a. We find a monotonic increase of the optical gap with the fraction of sulfur in the film.

In order to understand the possible microstructure of our films, we perform density functional theory (DFT) calculations using supercells consisting of (6 × 6) TMD unit cells in a periodic arrangement (further details in the supporting information). For each sulfur-to-selenium ratio, we set up supercells that place the sulfur and selenium atoms in different relative locations on both the top and bottom chalcogen plane; we then identify the arrangement with the lowest formation energy. Most of $MoS_{2(1-x)}Se_{2x}$ structures are found to have a very slight negative formation energies (for x = 1/3, 1/2, and 2/3, the formation energies are the lowest at -6, -7, and -

5 meV per $MoS_{2(1-x)}Se_{2x}$ unit), indicating the preference of these structures over the segregation of MoS_2 and $MoSe_2$ even at zero temperature. This behavior has been analyzed in detail in an earlier study by Kang *et al.* [53] Given the influence of entropy, random alloys are expected to be highly stable at elevated temperatures. Phonon dispersions for the case x=1/3, 1/2, and 2/3 confirm calculated with VASP[54] and Phonopy[55] confirm that there is no unstable mode, indicating again that the $MoS_{2(1-x)}Se_{2x}$ alloy structures are stable.

For each optimized structure, we calculate the electronic band structure. We find a direct band gap for all cases. As in prior DFT work,[53] our calculations underestimate the band gap (MoS_2: 1.68 eV/1.55 eV, $MoSe_2$: 1.45 eV/1.28 eV excluding/including spin-orbit interactions). The computational gaps scale approximately linearly with the S/Se ratio (the supporting material includes a figure showing the composition-dependent bandgap including and excluding spin-orbit interactions). This linear behavior suggests the linear prediction indicated by the black line in Fig. 5-2b, which is based on the experimental values of the optical bandgaps of MoS_2 and $MoSe_2$. We note that a statistical distribution of chalcogen atoms in the material may present source of deviation from this linear behavior: excitons created in CVD grown MoS_2 have been shown to have a short (a few unit cells)[56] but finite diffusion length and are expected to be attracted to areas of higher local Se content where the bandgap and their energy is lower. Statistical fluctuations in lower-dimensional materials like our 2D layers are more significant than in typical 3D alloys and the supporting material outlines how this can have an impact on the apparent

optical bandgap.

To further characterize the homogeneity of the grown films, we obtained spatial maps of the optical bandgap of several samples of different composition using a Horiba LabRam instrument with 10x/100x objectives for mapping of areas larger/smaller than 50 μm × 50 μm, respectively. Fig. 5-2a shows a set of typical PL spectra acquired on a 5 μm grid across a 20 μm × 20 μm area. No meaningful variation is observed. Subtraction of a linear background and subsequent Gaussian fitting of such sets of spectra provides the spatial maps of the optical bandgap, displayed for three different compositions in a false color representation in Fig. 5-2b. On the scale of the tuning range of the optical bandgap, the spatial variation is indiscernible. Fig. 5-2c provides higher energy resolution and shows the variation of the optical bandgap across regions of 70 μm × 70 μm area (top) and a 5 μm × 5 μm (bottom) size. We find a mean value of 1.713 eV and a variation of ±2 meV for the data on the larger spatial scale, for which the excitation spot size was ~ 5 μm in diameter. For the finer spatial map with 0.5 μm resolution, we observe a variation of ±5 meV, which appears to be correlated with the presence of individual crystalline domains. Based on the near-linear variation of the bandgap with composition (Fig. 5-1b), this variation, if it arises solely from a compositional variation, would correspond to of ±1% on the larger and ± 3% on the finer scale.

Variation in doping, strain or other substrate effects might also contribute to the observed variation. Fig. 5-3 shows a map of the of the PL center energy obtained on an isolated alloy island in the periphery of a single-layer film; its triangular shape

indicates that it is likely single-crystalline. We find that the overall PL energy of the island closely matches that of the adjacent film. There is a slightly increased/decrease of PL photon energy at the outside edges and inside of the island (±15 meV), respectively. In any case, fluctuations of ± 2 meV, ± 5 meV or even 15 meV represent a small fraction of the total tuning range of 320 meV and are indicative of the large-scale homogeneity and the absence of significant phase segregation in our films.

As a further characterization of our alloy films, we have measured the temperature dependence of the PL. The $MoS_{0.42}Se_{1.58}$ monolayer of Fig. 5-3 exhibits typical behavior, with the optical gap E_g decreasing with temperature. The results can described using the semi-empirical formula of O'Donnell et al.[57]:

$$E_g(\mathrm{T}) = E_g(\mathrm{T}=0) - S\langle\hbar\omega\rangle\,[coth(\langle\hbar\omega\rangle/2k_BT)\text{-}1] \qquad (1)$$

The fit implies an optical band gap at zero temperature $E_g(T=0)$ = 1.70 eV, an electron-phonon-coupling parameter of S = 1.98, and an average acoustic phonon energy of $\langle\hbar\omega\rangle$ = 17.0 meV for $MoS_{0.42}Se_{1.58}$. These values compare reasonably with the results for pure MoS_2 (1.86 eV, 1.82 and 22.5 meV) and $MoSe_2$ (1.64 eV, 1.93, 11.6 meV) reported by Tongay *et al*.[58].

We have measured Raman spectra of films of different compositions (Fig. 5-5a) by means of the same instrument and excitation wavelength (532 nm) as used for the PL measurements. The experimental Raman spectra of the $MoS_{2(1-x)}Se_{2x}$ monolayer films show two distinct sets of features, with one set related to MoS_2-like E_{2g} and A_{1g} modes at around 400 cm^{-1} and the other set related to the corresponding $MoSe_2$-like features near 240 cm^{-1}.

Unlike the bandgap, which is expected to vary smoothly with composition, the vibrational behavior of alloys is seen to be more complex than that of the stoichiometric compounds. The spectra represent a typical "two-mode behavior" (2MB) as it is also observed, for instance, in in AlGaAs, InGaP and Si-Ge alloy., and it does not indicate phase separation. 2MB occurs when the Raman frequency shifts of compounds AB and AC differ greatly, which – at ~200 cm^{-1} – is indeed the case for $MoS_{2(1-x)}Se_{2x}$, but not for $Mo_{(1-x)}W_xS_2$ alloys, for which the difference is less than 50 cm^{-1} resulting in a continuous shift of the Raman line typical for a "one-mode behavior".[59]

We have also performed spatial mapping of the Raman response across the area shown in the bottom of Fig. 5-2c (i.e., over a grid at 0.5 μm spacing). Fig. 5-5b is the hypersurface created by plotting the Raman spectra against a coordinate indicating the spatial location on the sample. The spectra are normalized to the intensity at 400 cm^{-1}; the pronounced feature on the right is the substrate SiO_2 mode. No meaningful variation of the Raman spectra with position is discernible, in good agreement with the homogeneity found for the PL signal in Fig. 5-2c.

In conclusion, we have shown the ability to grow $MoS_{2(1-x)}Se_{2x}$ films and that the optical bandgap in the resultant films can be tuned at will by the S/Se ratio. Future work will address the electrical transport properties of monolayer $MoS_{2(1-x)}Se_{2x}$ films and the influence of alloying on the transport characteristics. Another important fundamental property of the alloys is the variation of the spin-orbit splitting of the bands, which is predicted to increase continuously with increasing Se content, and the

implications of this variation for spin manipulation.

5.4 Figure

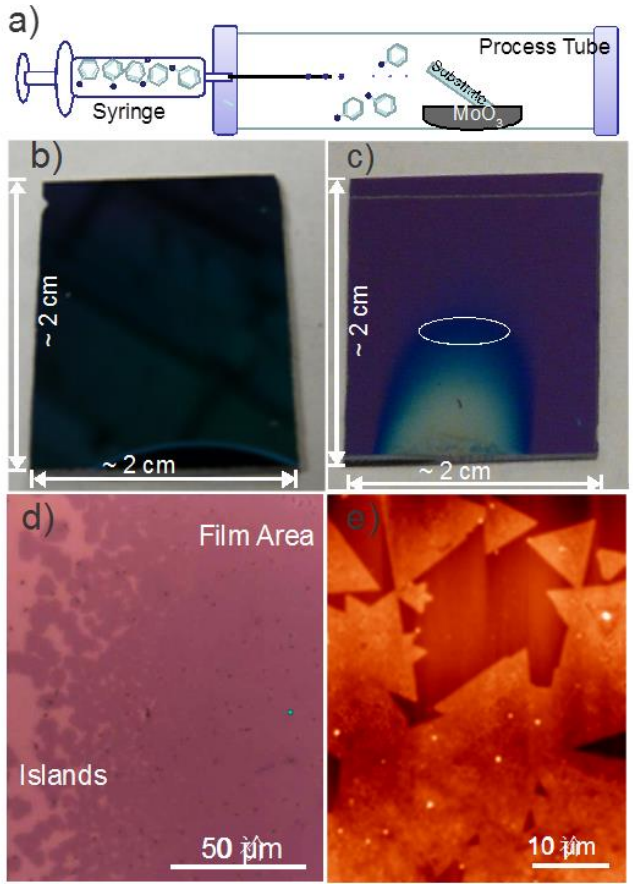

Figure 5-1: a) Schematic representation of the growth mode: a substrate is suspended above MoO_3 and heated in a tube furnace to 650-700°C in nitrogen, at which point liquid chalcogen precursors are injected. b,c) Optical images of MoS_2 and $MoSe_2$ single-layer films on 300nm SiO_2/Si substrates, respectively. A single-layer MoS_2 film covers the entire substrate except the dark area at the bottom. Homogeneous single-layer growth of $MoSe_2$ is found in the circled area of the substrate. d) optical micrograph of the area near an edge of an $MoS_{1.5}Se_{0.5}$ film. While on the left, individual mostly triangular islands are visible, the actual film area (on the right) is continuous and presumably contains many rotational domains. e) Representative AFM image of the area near the edge of an alloy film showing triangular single-layer islands (top, ~0.8 nm in height) that merge into a continuous film (bottom)

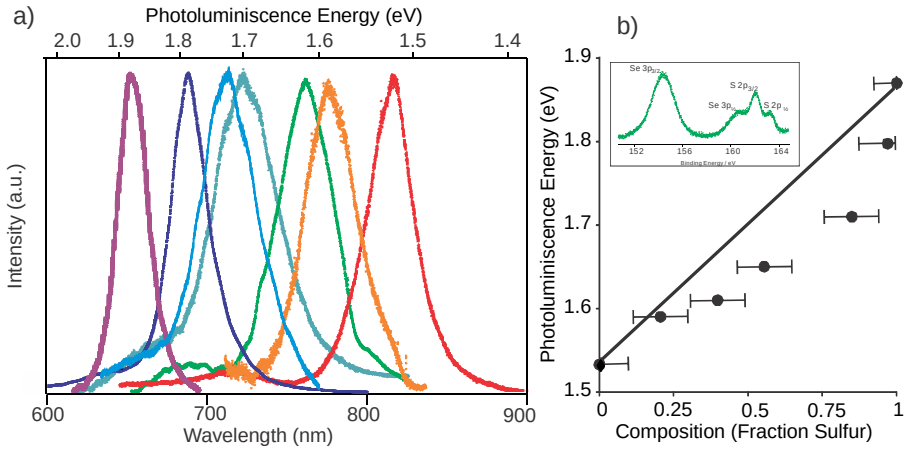

Figure 5-2: (a) Normalized RT PL spectra for $MoS_{2(1-x)}Se_{2x}$ films of different composition. (b) Variation of the PL photon energy as a function of sample composition, as determined by XPS (the inset shows a representative XPS spectrum of the Se 3p and S 2p peaks). The black line indicates a linear variation between the values of the unalloyed compounds; a linear variation is also found in DFT calculations.

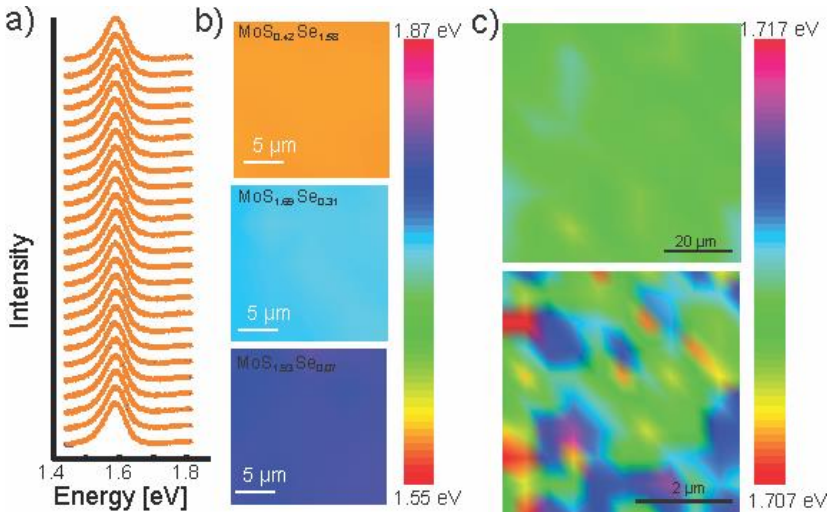

Figure 5-3: (a) PL spectra obtained on a regular grid across a 20 µm × 20 µm area of a $MoS_{0.42}Se_{1.68}$ alloy monolayer. (b) False color spatial maps of the optical bandgap obtained by fitting PL spectra like in (a) with a Gaussian function. Compared to the range of achievable optical band gaps, no meaningful spatial variation in the emission energy is observed. (c) The spatial variation of the optical bandgap across a 70 µm × 70 µm area (top) and a 5 µm × 5 µm area (bottom) using a spot sizes of ~5 µm and 0.5 µm, respectively. On the larger scale the variation is ± 2 meV; this would corresponds to ~ ±1% of compositional variation. On the finer scale, where individual crystalline domains are visible, the variation is ± 5 meV (~ ± 3 % compositional variation).

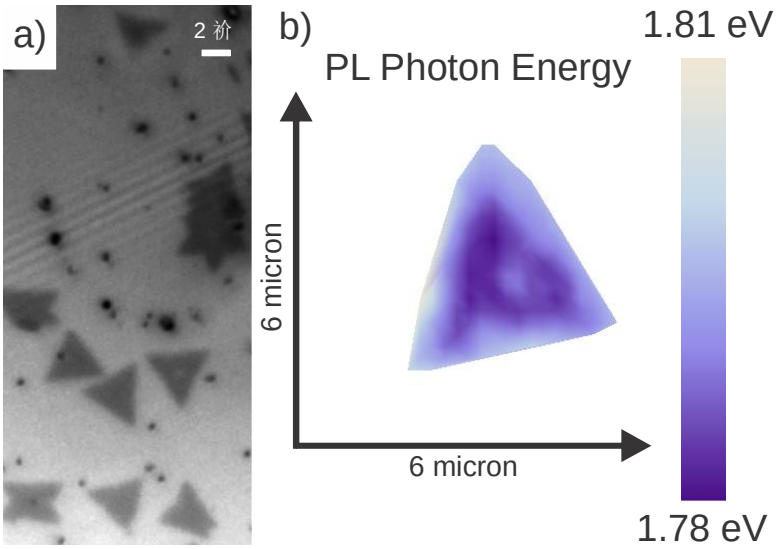

Figure 5-4:: a) Optical image of several triangular $MoS_{1.5}Se_{0.5}$ islands on our SiO_2/Si substrate. b) Spatial mapping of the photon energy of one of the islands measured with 200-nm step size using a 100x objective and 532 nm excitation. The island exhibits the lowest photon energy at its center and it rises slightly toward the perimeter. The color scale shows a variation of 30 meV

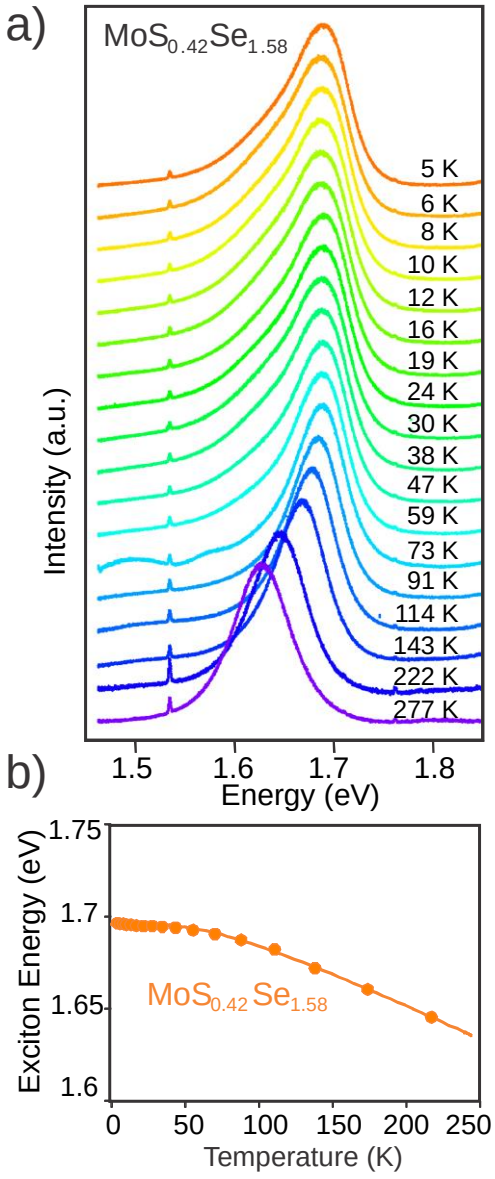

Figure 5-5: (a) PL spectra for a $MoS_{0.42}Se_{1.58}$ film (orange in Fig. 5-2a) at different temperatures between 277 and 5 K. All spectra are scaled to the same height. (b) The exciton emission energy (obtained from a Gaussian fit of the PL spectra) as a function of the temperature of the film. The fit (solid line) is described in the text.

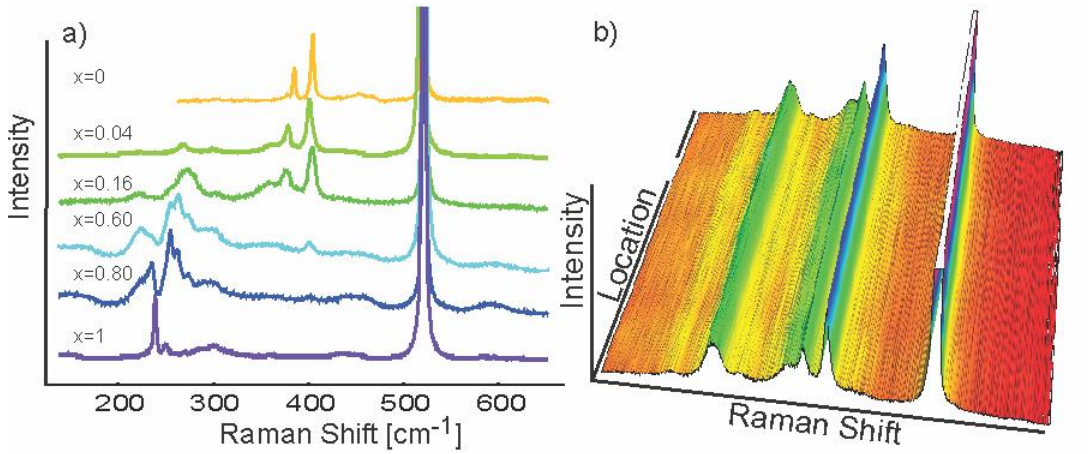

Figure 5-6: a) Raman spectra measured for $MoS_{2(1-x)}Se_{2x}$ films of different selenium content *x*. The pronounced feature near 520 cm^{-1} arises from the SiO_2 substrate vibrations. While the peak patterns for the pure materials are simple and sharp, the patterns for alloy films are broader and more complex. b) Three-dimensional representation of the Raman spectra as a function of location on a 0.5 μm grid covering the same location as the bottom part of Fig. 5-2c of the main text.

Chapter 6 Facile Growth of Monolayer MoS_2 Film areas on SiO_2/Si

The following is taken from an article that published in The European Physical Journal B: Mann, J., Sun D., Ma, Q., Chen, J., Preciado, E., Ohta, T., Diaconescu, B., Yamaguchi, K., Tran, T., Wurch, M., Magnone, K., Heinz, T., Kellogg, G., Kawakami, R and Bartels, L., Facile growth of monolayer MoS_2 film areas on SiO_2, 10.1140/epjb/e2013-31011-y. This was collaborative work with Scientists in Sandia national Laboratory and postdoc at Columbia University.

6.1 Overview

In this chapter, we show that the preparation of MoS_2 can be achieved in a very facile manner. Past examples of MoS_2 growth started from thin PVD Mo layers [12] or impregnation of a substrate in a Mo-containing solution[50] followed by sulfurization , as well as the simultaneous deposition of molybdenum (typically from a MoO_3 source) and elemental sulfur[60]. In this section, we follow the latter avenue and show that the fabrication of films hundreds of microns across can be achieved with minimal control of the growth conditions. The films are uniform in their spectroscopic properties and feature large areas that are exclusively monolayer in thickness. In this chapter we provide photoluminescence (PL), Raman spectroscopy, low-energy electron diffraction (LEED), atomic force microscopy (AFM) and x-ray photoelectron spectroscopy (XPS), and transport measurements to validate the quality of our films.

6.2 Materials and Methods

We use two alumina crucibles (Aldrich Z561738, 70 mm × 14 mm × 10 mm) containing MoO_3 (Aldrich 99.5%) and sulfur (Alfa 99.5%) powder and as Mo and S sources respectively. These sources are placed in a quartz process tube (2" diameter), which is inserted in a three-zone tube furnace (Mellen TT12) of which exclusively the center zone is operated. Nitrogen gas (99.999%) is used to purge the tube and offered at a rate of 5 SCFH during growth. The MoO_3 crucible is placed at the center of the heated zone and the sulfur crucible is placed upstream, outside the operated zone of the tube furnace. Our substrate is a 3×3 cm pieces of a boron-doped Si(110) wafer carrying 300 nm of oxide (SUMCO). It is cleaned by Piranha etch using a mixture of 3 parts sulfuric acid and 1 part hydrogen peroxide (40%) immediately before use. We subsequently applied an O_2 plasma etch on some samples, yet we found similar results without its use. During heat-up of the furnace, optimization of the distance between the crucibles allows us to reach approximately 880K (as measured by a type K thermocouple) at the outer surface of the process tube at the location of the MoO_3 crucible at the same time as the sulfur melts into a clear liquid with a flat uniform surface. We find that the duration that the substrate is exposed to the fumes from the liquid sulfur is crucial in determining the structures we grow. We achieved the results shown here by waiting for 3 minutes after the sulfur melts. Subsequently, all power to the furnace is switched off and it is left to cool while continuing the N_2 flow. Thus, no temperature control of the furnace is needed. Fig. 6-1a shows the temperature transient and the supporting information includes a photo

of the process tube with the sulfur and MoO_3 crucibles.

6.3 Results and Discussion

Post deposition, the substrates carry elongated areas hundreds of microns long and ≈100 microns across (Fig. 6-1b) that are homogenously covered by a MoS_2 monolayer film. At its edge, the film disintegrates into isolated, mostly-triangular islands (Fig. 6-1c), which exhibit identical spectroscopic and morphological characteristics as the film (vide infra). Other places on the substrate are covered by triangular multilayer MoS_2 islands (see supporting info) or no material at all. We also find thicker MoS_2 films predominantly surrounding areas with substrate point defects. The resultant film is stable in air for weeks. Atomic force microscopy shows the film interrupted by a small number of isolated irregular pits. No dislocation lines or 2D grain boundaries can be resolved. From the triangular shape of many of the island at the film perimeter, we assume that these do not contain grain boundaries, which suggests a minimum grain size on the order of 10 microns for the continuous film.

Selected area XPS measurements (Fig. 6-2) using a Mg K-α source and a VG Scientia 300 analyzer show on the film the sulfur 2s and molybdenum 3d 3/2 and 5/2 peaks at 226.1, 228.8, and 232.0 eV, respectively, as expected for S^{2-} and Mo^{4+}. We referenced the spectrum to the substrate silicon peaks and the values mentioned are in good agreement to the reference values published by NIST for bulk MoS_2 [61]. While we can find areas on the sample which show also peaks/shoulders

corresponding to a higher oxidation state of molybdenum (Mo^{6+}, indicative of MoO_3) as shown in Ref. [12], the film area and the monolayer islands do not feature them. These measurements confirm that the films we produce are comprised of pure MoS_2.

For Raman spectroscopy (Fig. 6-3a) we use a 532 nm cw laser at 0.1 mW in a spot size of ≈1 micron. The spectrum shows the E_{2g} and A_{1g} peaks of MoS_2 at 384 and 405 cm^{-1} and the silicon substrate peak at 520 cm^{-1}. The separation of the E_{2g} and A_{1g} peaks can be used to identify the MoS_2 film thickness. We find a value of 20.9 cm^{-1} that is in good agreement with prior measurements on CVD grown MoS_2 [12, 50, 60, 62] and between the values observed for monolayer and bilayer exfoliated MoS_2 [63]. The Raman peak position and separation is uniform across our film areas. Mapping the sample in a 1 micron grid, we observe variations ≤0.3 cm^{-1} over an area >100 microns across (inset in Fig. 6-3a); the islands at the edge of the film area show a Raman signal identical to the center of the film, suggesting that their structure and composition is not different from the extended film.

Photoluminescence measurements (Fig. 6-3b) use the same excitation source and conditions as the Raman spectroscopy. We find a single peak at 1.87 eV. This peak corresponds to the direct band gap transition of monolayer material[14, 64]. The photoluminescence yield was about twice as high as what we find for MoS_2 monolayers exfoliated on SiO_2. Mapping of the continuous film and the area where it transitions into individual islands shows no difference in peak position, even on the islands, indicating that they are formed of the same material.

We also fabricated a total of 5 contacts on an MoS_2 island (see supporting

material for a picture) and measured I-V curves (Fig. 6-4) in a 4-point probe setup across a 2 micron gap as a function of a gate voltage applied to the silicon substrate (no gate leakage was detected). The curves acquired with a Keithley 2400 source meter and a Keithley 2002 multimeter reveal an n-doped material; as it is most commonly found for exfoliated and deposited MoS_2 films [50, 65-70]. We speculate that this behavior is caused by sulfur vacancies in the film and that further optimization of the growth process can reduce it. Application of gate voltages up to -100 V (at nominally 300 nm oxide thickness) was insufficient to render the device ambipolar. We measured a mobility of 0.26 $cm^2 V^{-1} s^{-1}$, in good agreement with many previous measurements of similar MoS_2 samples [50, 65-67].

Attempts at SEM imaging of the film on the substrate were not successful, likely due to charging effects. Release or transfer of the material from our substrates was not attempted to date.

In summary, we show that by very simple means and without temperature control MoS_2 monolayers of almost a millimeter across can be fabricated. The resultant films show exclusive monolayer behavior and excellent uniformity in their photoluminescence and Raman signal. Future research will address the chemical and catalytic properties of thus prepared films.

6.4 Figure

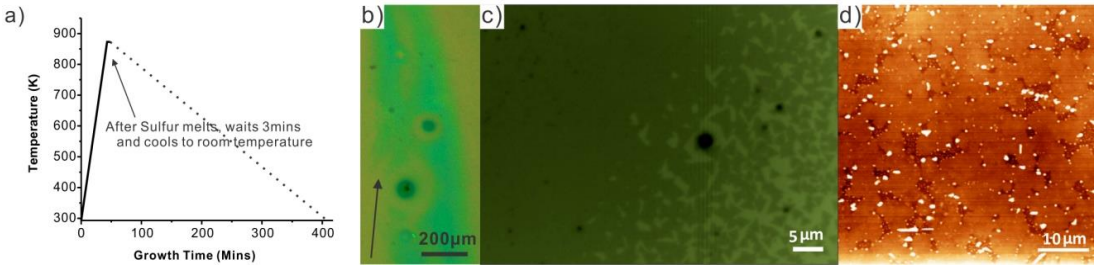

Figure 6-1: a) Approximate temperature transient during MoS_2 growth consisting of powering the furnace until 3 minutes after the sulfur is molten and subsequently switching it off. b) optical microscope image of MoS_2 film on the substrate. The N_2 flow direction is indicated. c) at its edge, the MoS_2 film disintegrates into individual flakes of mostly triangular geometry. d) atomic force image on the film area in air shows a continuous film with a small number of irregular shaped pits. No domain boundaries could be resolved.

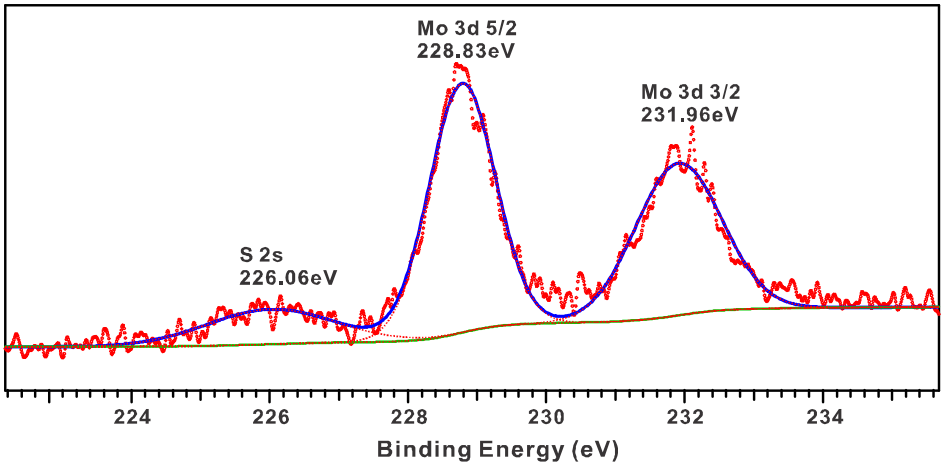

Figure 6-2: X-ray photoelectron spectroscopy of the Mo 3d and S 2s peaks on MoS_2 films on SiO_2/Si substrate; the S 2p peaks overlap with signal from the Si substrate.

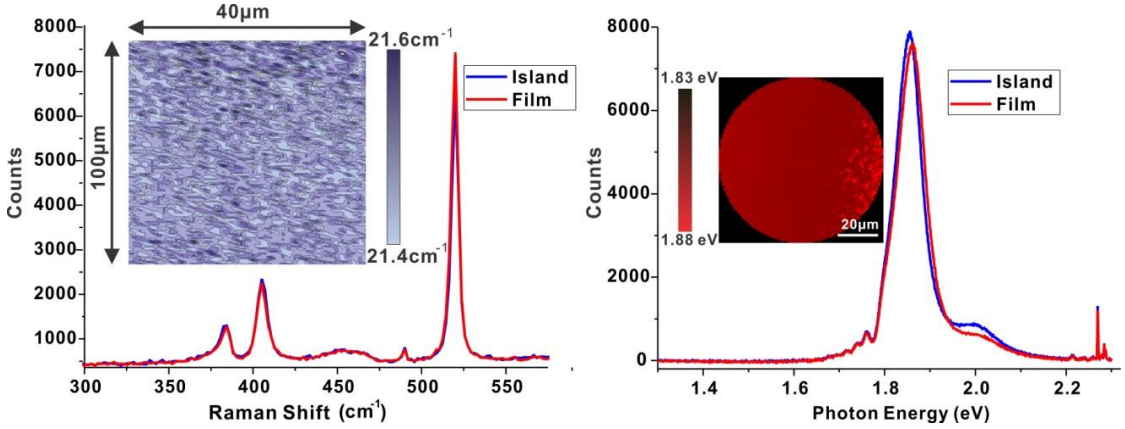

Figure 6-3 a): Raman spectrum of MoS_2 film and island: two characteristic peaks located at 384.3 and 405.2 corresponding to MoS_2 E^1_{2g} and A_{1g} vibrational modes. The inset shows mapping of the frequency difference between the E^1_{2g} and A_{1g}. Its variation of ≤ 0.2 cm $^{-1}$ attests high uniformity of the film. Fig 6-3b): Photoluminescence spectrum of the MoS_2 film for both continuous film and individual islands nearby show an identical single peak at 1.87 eV. The insets show the mapping data from the edge of the continuous film (left) to an area covered partly by island (right).

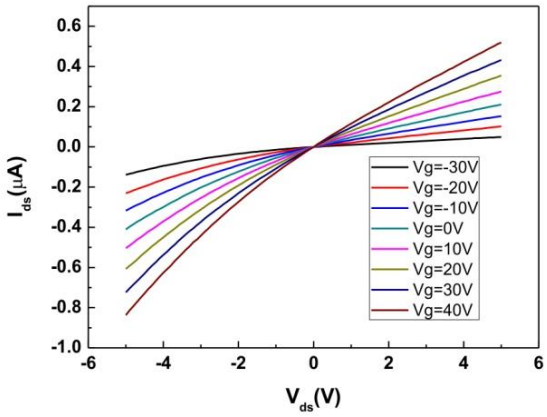

Figure 6-4: Current-Voltage (I-V) measurements in a 4-probe setup across a 2 micron gap at the edge of our monolayer MoS_2 film for different gate voltages (V_g). The conductivity increases with positive gate voltages indicating an n-type material.

Chapter 7 Symmetry Resolved Surface-Derived Electronic Structure of MoS2(0001)

The following is taken from an article that has been submitted to Journal of Physics: Condensed Matter: Takashi Komesua, Duy Le, Quan Ma, Eike F. Schwier, Yohei Kojimae, Mingtian Zheng, Hideaki Iwasawa, Kenya Shimada, Masaki Taniguchid, Ludwig Bartels, Talat Rahman and P. A. Dowben, Symmetry Resolved Surface-Derived Electronic Structure of MoS_2(0001). This was collaborative work performed at the linear undulator beamline (BL-1) of the Hiroshima Synchrotron Radiation Center (HiSOR) at Hiroshima University, Japan. ARPES measurements were done by Dr. Takashi Komesua, Dr. Eike Schwier and I. Computational support came from Dr. Duy Le of the University of Central Florida.

7.1 Overview

This study reports high-resolution angle resolved photoemission spectroscopy (ARPES) characterizing the electronic band symmetry and wave vector dependence of the band symmetries for MoS_2(0001). We compare the symmetry resolved experimental band structure to density function theory (DFT) results to extract the spectral weight contributions to the band structure as a function of wave vector. Band symmetry would not, *a priori*, be expected along the line from $\bar{\Gamma}$, the surface Brillouin zone center (SBZ), to the $\bar{K}$ point at the surface Brillouin zone edge

because the $MoS_2(0001)$ surface is C_{3v} symmetry, not C_{6v} symmetry, and the direction from $\bar{\Gamma}$ to the $\bar{K}$ point retains no true mirror plane symmetry away from $\bar{\Gamma}$, the Brillouin zone center. Yet we find that, in spite of limited symmetry, the effect of photoemission symmetry selection rules generally still applies in our spectra.

7.2 Experimental

The high-resolution angle-resolved photoemission spectroscopy (ARPES) was performed at the linear undulator beamline (BL-1) [71] of the Hiroshima Synchrotron Radiation Center (HiSOR) at Hiroshima University, Japan. We measured along the line from $\bar{\Gamma}$-$\bar{K}$ line in p-polarization (the incident light vector potential $\underline{A}$ parallel to the mirror plane) and s-polarization geometry (the incident light vector potential $\underline{A}$ perpendicular to the mirror plane) to distinguish initial valence band states with even and odd symmetries with respect to the nominal $\bar{\Gamma}$-$\bar{K}$ line mirror plane [72]. The ARPES experiments were carried out using an angular (display) mode of the hemispherical electron analyzer (R4000, VG-Scienta) with an acceptance angle of ±15°. We used several different incident photon energies focusing on results obtained at $h\nu$= 34 eV and 75 eV. The energy resolution was limited by temperature, not the instrument, and estimated to be about 30 meV as the ARPES was performed at room temperature. Throughout the discussion, the binding energies are referenced to the Fermi level ($E_F - E$) of an Au film electrically

connected to the sample.

The surface of the $MoS_2(0001)$ sample was prepared by cleaving a bulk crystal *in-situ* at a base pressure of better than 10^{-10} Torr. The surface quality and periodicity was ascertained by low energy electron diffraction (LEED), as in Figure 7-1b, and photoemission. The low energy electron diffraction (LEED patterns), of the $MoS_2(0001)$ surface, such as those taken at an incident electron energy 117.8 eV, provided a means to determine the orientation of the 2-dimensional surface Brillouin zone, independent of ARPES. The orientation of the $MoS_2(0001)$ samples was further validated by iso-kinetic energy wave vector dependent photoemission intensity plots. Figure 7-1c and 7-1d illustrates the line of surface Brillouin Zone (SBZ), from the SBZ center ($\bar{\Gamma}$) to the SBZ edge at $\overline{K}$ and $\overline{M}$ near the top and bottom of the valence band, respectively. These measurements serve as the basis for the placement of the nominally high symmetry points $\overline{K}$, $\overline{M}$ and $\overline{M}$' at the SBZ edge. Due to small misalignments and/or faceting, multiple samples and multiple surfaces were prepared.

7.3 Theoretical methodology

We performed spin-polarized density functional theory (DFT) calculations using the super cell method with a plane-wave basis set (at a cut-off energy of 500 eV) and the projector-augmented wave (PAW) [73, 74] technique as implemented in the Vienna *ab-initio* Simulation Package (VASP) [75, 76]. We applied the generalized gradient approximation (GGA) in the form of Perdew-Burke-Ernzerhof

(PBE) functional [77] to better describe the exchange-correlation of the electrons together with the pairwise DFT-D3 correction [78] for better accounting of van der Waals (vdW) interactions. The Brillouin Zone was sampled for bulk MoS_2 and the MoS_2(0001) surface with (18 × 18 × 6) and (15 × 15 × 1) k-point meshes, respectively. The optimized lattice parameter and the interlayer distance of MoS_2 are found to be 3.158 Å and 6.143 Å, respectively, in excellent agreements with experimental data [79-81]. For modelling the MoS_2(0001) surface, we use a 10 layer slab of the MoS_2 trilayer.

The electronic band structure along the $\bar{\Gamma}$-$\bar{K}$-$\bar{M}$-$\bar{\Gamma}$ directions were calculated with 159 k-points and then projected onto every orbital of each atom to resolve the symmetry characters of the corresponding wave-functions (i.e. their *l* and *m* numbers). Subsequently, we sum all projections that correspond to even or odd symmetries with respect to the mirror plane.

Symmetry selection along a low symmetry line surface Brillouin zone ($\bar{\Gamma}$-$\bar{K}$)

Utilization of linearly polarized light from a synchrotron light sources, enables us to exploit the dipole selection rules for the photoemission process and allows us to clarify the symmetry properties of the electronic states in solids [72]. The point group symmetry of the MoS_2(0001) surface is C_{3v}, and consequently C_{3v} is the point group symmetry applicable at $\bar{\Gamma}$ while C_{2v} characterizes $\bar{M}$ and C_{1h} applies along the high-symmetry directions ($\bar{\Gamma}$-$\bar{M}$). There is no mirror plane symmetry at both the $\bar{K}$ point and along the $\bar{\Gamma}$-$\bar{K}$ line In contrast, if the applicable point group

symmetry were C_{6v} then C_{6v} would apply at $\overline{\Gamma}$, C_{3v} at $\overline{K}$, C_{2v} at $\overline{M}$,and C_{1h} along the two high-symmetry directions ($\overline{\Gamma}$-$\overline{K}$ and $\overline{\Gamma}$-$\overline{M}$). Such a reduction of symmetry generally has important consequences: for instance in graphene, symmetry reduction from C_{6v} to C_{3v} results in the loss of the Dirac point and opening of a band gap on a number of different substrates [82].

Assuming that the final state of photoemission can be described by a plane wave traveling to the photoelectron analyzer, the photoelectrons in the final state transform as the fully symmetric representation in both C_{3v} and C_{1h}. Under this assumption, we can determine the symmetry of the initial states based on the general photoemission transition rules and compare them to theoretical predictions of the orbital character of the various MoS_2(0001) valence bands. The photoemission transitions rules are based on the orientation of the incident photon vector potential the electronic band character, well known as Fermi's Golden rule exploiting the point group representation, (irreducible representations), each crystallographic symmetry, such as C_{1h}, C_{2v} C_{3v}.

We find experimentally a band structure that clearly differs for states of even and odd symmetry, based on the atomic orbital rectangular representation, in spite of an overall low symmetry along the $\overline{\Gamma}$ to $\overline{K}$ line of the surface Brillouin zone for MoS_2(0001), even away from the high symmetry $\overline{\Gamma}$ point. Figure 7-2 illustrates the calculated theoretical band structure, both for the bulk (Figure 7-2a) and the surface (Figure 7-2b) for nominally even states as compared to states of even symmetry in the experimental (Figure 7-2c) band structure (the p-polarized setting), were the $\overline{\Gamma}$

to $\overline{K}$ line mirror plane present. This band structure (Figure 7-2) differs significantly from the calculated theoretical band structure, both for bulk (Figure 7-3a) and surface (Figure 7-3b) for nominally odd states, even compared to the experimental (Figure 7-3c) band structure (the s-polarized setting), that would probe only odd states were the mirror plane present. Fig. 7-3 shows odd states of theoretical and experimental (s-polarized setting) results. At higher photon energies (75 eV, instead of 34 eV), the results are qualitatively similar: states of even and odd symmetry, based on orbital symmetry, can be distinguished in the experimental band structure (Figure 7-4) taken with p-polarized light (Figure 7-4a) and s-polarized light (Figure 7-4c), in spite of the absence of the mirror plane symmetry along the $\overline{\Gamma}$ - $\overline{K}$ line, away from the Brillouin zone center. For the data taken at the high photon energy of 75 eV, the agreement between theory and experiment, based on even and odd symmetry states, were the mirror plane symmetry present is excellent, as illustrated in Figure 7-4b and Figure 7-4d respectively. This agreement between theory and experiments is also seen at the lower photon energy of 34 eV for the band structure made of states of nominally even symmetry, as seen in Figure 7-2d. The nominally even states, especially those states in the bands near the top of the valence band as well as those weak bands around 1 eV greater binding energy, as seen in Figure 7-2b, are in good agreement with the experimental results of Figure 7-2c and clearly overlap as illustrated in Figure 7-2d. But the agreement between theory and experiments is not universal, as seen for the band structure made of states of nominally odd symmetry, for the data taken the lower photon energy of 34 eV

(Figure 7-3d).

Wave vector dependent spectral weight contributions along the low symmetry $\overline{\Gamma}$ - $\overline{K}$ line of surface Brillouin zone

We note that in Figures 7-2 and 7-3, the calculated band structures differ little for the bulk and surface states, not unreasonable for a layered system were the interactions between layers are dominated by weak van der Waals interactions. Yet the spectral contributions to the band structure by the atomic states separated by azimuthal and polar quantum numbers (angular momentum quantum number *l* and magnetic quantum number *m*) are indeed wave vector dependent. Figure 7-5 shows the calculated band states (surface and bulk) with selected angular momentum values *l* and *m*, which aids in the identification of the orbital character weights in the experimental band structure separated by states of even symmetry (Figure 7-5a through 7-5f) and odd symmetry (Figure 7-5g through 7-5i), if one assumes that mirror plane symmetry along the $\overline{\Gamma}$ - $\overline{K}$ line were preserved.

Based on this symmetry assignment, one cannot only see clear differences between the band structure of made even and odd states, as seen in Figure 7-2 and Figure 7-3 respectively (and Figures 7-4a,b and Figures 7-4c,d respectively), but Figure 7-5 implies that the spectral weight contributions are indeed wave vector dependent. Through a comparison of the individual orbital contributions, as noted and partially illustrated in Figure 7-5, with experiment, it is clear that those bands close to the valence band maximum (i.e. closest to the Fermi level) at near $\overline{\Gamma}$ point, are nominally even states of Mo $4d_{3z^2\text{-}r^2}$ character, i.e. (*l*, *m*) = (2, 0) (Figure 7-5c),

hybridized with states of states of *s* character, i.e. (*l*, *m*) = (0, 0) (Figure 7-5a). Similarly, the bands at the bottom of the valence band, i.e. at the higher binding energy of about -6 eV and -7 eV, are again dominated by states d_{3z2-r2} character, i.e. (*l*, *m*) = (2, 0) (Figure 5c), and *s* character, i.e. (*l*, *m*) = (0, 0) (Figure 7-2a) near $\bar{\Gamma}$ point, in even symmetry (Figure 7-2), hybridized with states of states p_z character of (1, 0) (Figure 7-5b). We note that the experimentally derived band dispersions agree reasonably well with the DFT derived band structures for both even and odd symmetries (Figures 7-2, 7-3 and 7-4).

Near $\bar{K}$ point, the top of the valence band is dominated by Mo d states of both even and odd symmetry, consistent with the expectation that away from the $\bar{\Gamma}$ point, given the low symmetry environment, both nominally even and odd states can hybridize, and given the shared spectral weight intensity at similar wave vector and binding energy, this is indeed the case. Overall, from Figure 7-5 and the generally excellent agreement between theory and experiment, we see that the Mo 5*d* states dominate at the top of the valence band and the sulfur 3*p* dominate at the bottom of the valence band. How then to explain the disagreement between theory and experiment near $\bar{K}$ point, in nominally even symmetry and at low photon energies (Figure 7-3).

The effects of low symmetry along $\bar{\Gamma}$ - $\bar{K}$ of the surface Brillioun zone

As noted above, the agreement between the experimental band structure and the calculated band structure is generally excellent except for the top of the valence

band, along the $\overline{\Gamma}$ - $\overline{K}$ line, as seen in the experimental band structure taken at the lower 34 eV photon energy (Figure 7-3d). Is this variation between theory and experiment the result of the loss of mirror plane symmetry at both $\overline{K}$ and along the $\overline{\Gamma}$ - $\overline{K}$ line that accompanies the reduction of the applicable point group symmetry were C_{6v} to C_{3v}, as suggested above. This loss of mirror plane symmetry at both $\overline{K}$ and along the $\overline{\Gamma}$ - $\overline{K}$ line that accompanies the reduction of the applicable point group symmetry were C_{6v} to C_{3v} is clearly evident in Figure 7-6, where the surface Brillouin zone has been overlaid on the low energy electron diffraction images of the MoS_2(0001) surface.

An in-plane Mo $4d_{x2-y2}$ (l=2, m=2) state contributed precisely what is missing from the theory in the comparison between the nominally odd symmetry band structure obtained from density function theory (DFT) and the experimental band structure obtained from angle resolved photoemission spectroscopy, for the s-polarization geometry and 34 eV photon energy along the $\overline{\Gamma}$ - $\overline{K}$ line. This is illustrated in Figure 7-7. The problem though is that the Mo $4d_{x2-y2}$ (l=2, m=2) state is of even symmetry were the mirror plane along the $\overline{\Gamma}$ - $\overline{K}$ line present. As this mirror plane symmetry is in fact absent, Mo $4d_{x2-y2}$ (l=2, m=2) state contributions can hybridize with the Mo $4d_{xy}$ (l=2, m=-2) odd state contributions, adding Mo $4d_{x2-y2}$ (l=2, m=2) state contributions to the top of the valence band, along the $\overline{\Gamma}$ - $\overline{K}$ line, as we can infer from Figures 7-7 and 7-3. A way to visualize this is to consider a state compatible with the d_{xy} function along the $\overline{\Gamma}$ - $\overline{K}$ line by inserting x = √3x'/2 -

y'/2 and y = x'/2 + √3y'/2, which in d_{xy} is proportional to a mixture of d_{xy} and $d_{x^2-y^2}$. Such an initial state would be strongly enhanced in s-polarized light as is observed. What is perhaps more surprising is the agreement between the experimentally derived band dispersion and the DFT band structures for the even and odd symmetries in spite of the absence of mirror plane symmetry along the $\bar{\Gamma}$-$\bar{K}$ line.

7.4 Conclusion

Surprisingly, in spite of an overall low symmetry along the $\bar{\Gamma}$ to $\bar{K}$ line of the surface Brillouin zone for MoS_2(0001), even away from the high symmetry $\bar{\Gamma}$ point, we find that generally photoemission symmetry selection rules are applicable according to the symmetry of the various atomic orbital contributions. The band structures are found to be significantly different for the states of even and odd reflection parities in spite of the negligible symmetry (no true mirror plane symmetry) along the $\bar{\Gamma}$ to $\bar{K}$ line of the surface Brillouin zone, even away from the high symmetry $\bar{\Gamma}$ point. These complications agree reasonably well with the density functional theory (DFT) calculation for each band symmetry, with one notable exception of Mo $4d_{x^2-y^2}$ (l=2, m=2) at some photon energies. The spectral weight contributions to the bands depend on the various atomic orbital contributions and their symmetry. These spectral weight contributions vary with wave vector and are different for different bands. This means that in spite of the low symmetry, the band structure MoS_2(0001), even away from the high symmetry $\bar{\Gamma}$ point. Overall, the

experimental band structure is the result of strong S 3p and Mo 4d hybridization with the top of the valence band is strongly dominated by Mo 4*d* while the bottom of the valence band is strongly dominated by Mo 5*s* and S 3p_z.

7.5 Figure

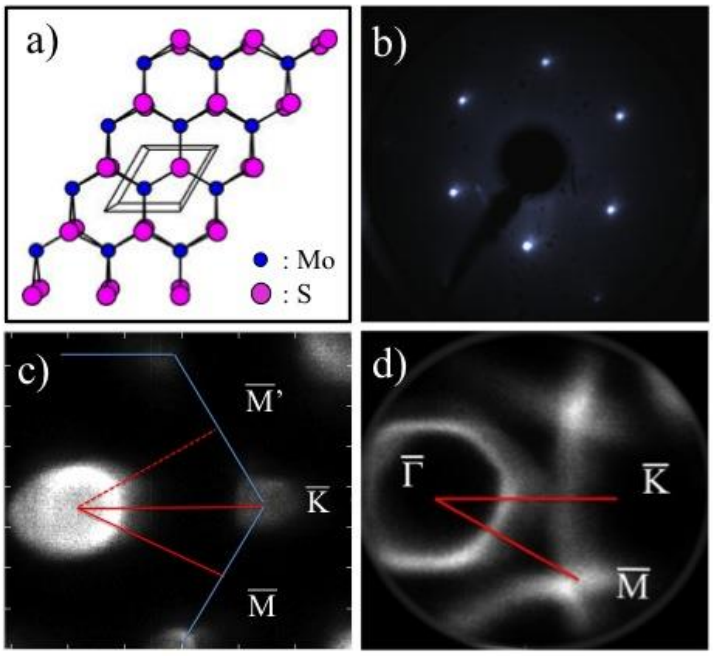

Figure 7-1: A schematic diagram of a MoS_2 layer (a), the low energy electron diffraction (LEED), of the MoS_2(0001) surface taken at an incident electron energy of 117.8 eV (b). The critical points ($\overline{\Gamma}$, $\overline{M}$, $\overline{K}$) of the 2-dimensional surface Brillouin zone can be inferred the experimental band structure, in this case from iso-kinetic energy wave vector dependent photoemission intensity plots. These wave vector dependent photoemission intensity plots were taken near the top of the valence band (c) and near the bottom of the valence band (d) using an incident photon energy of 34 eV. Those red lines indicate high symmetry lines of surface Brillouin Zone (SBZ), from the center of SBZ ($\overline{\Gamma}$) to the SBZ edge along different high symmetry lines ($\overline{\Gamma}$ to $\overline{M}$, $\overline{M}$' or $\overline{K}$).

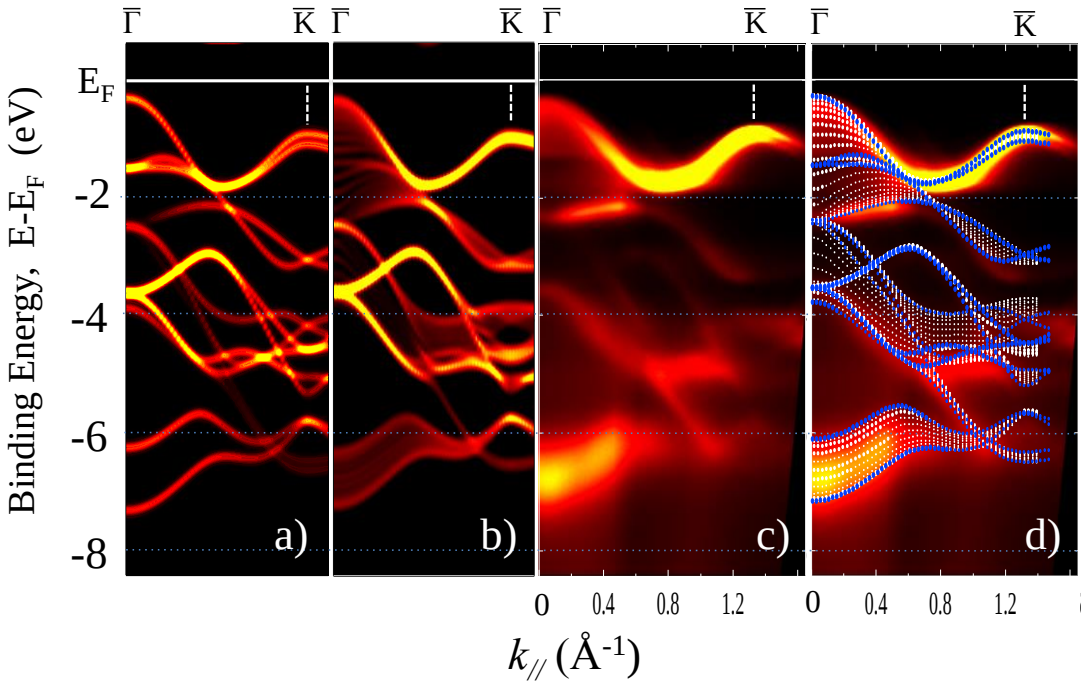

Figure 7-2: Comparison of the nominally even symmetry band structure (one that assumes mirror plane symmetry along the $\overline{\Gamma}$ - $\overline{K}$ line) obtained from density function theory (DFT) and experiment. The results of DFT theoretical calculation for surface (a) and bulk (b) of MoS_2(0001) respectively are compared to the display of the experimental band structure obtained from angle resolved photoemission spectroscopy, for the p-polarization geometry and 34 eV photon energy along the $\overline{\Gamma}$ - $\overline{K}$ line. The direct comparison is made on (d) with the DFT theoretical calculations overlapped with experimental results shown in (a), (b) and (c), with blue dots for surface states from (a), and white dots for bulk band states from (b).

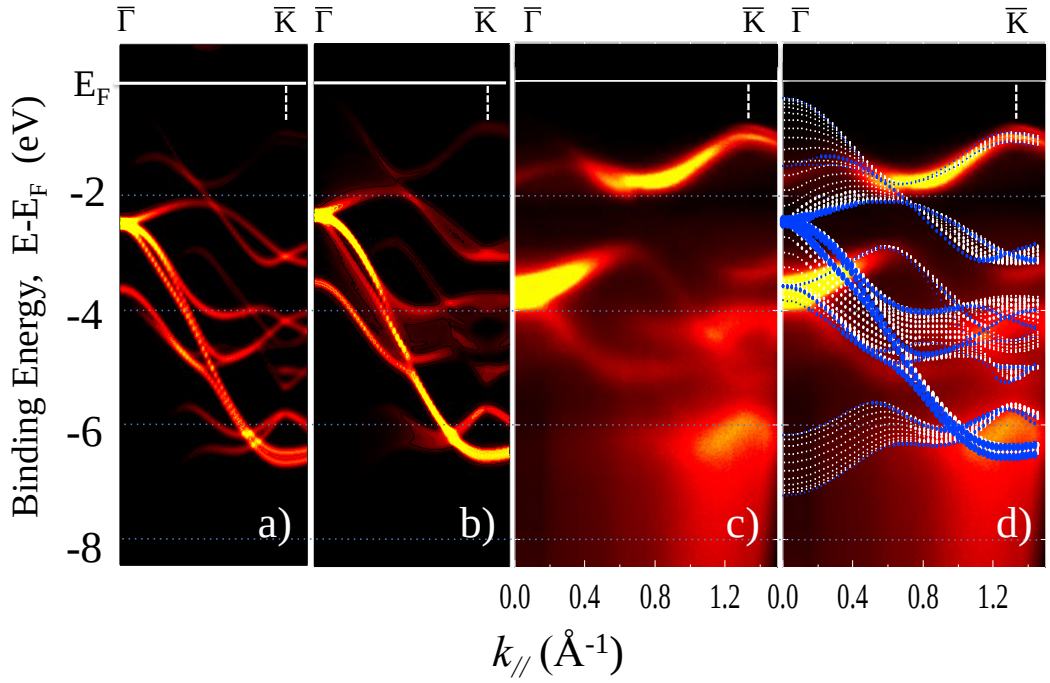

Figure 7-3: Comparison of the nominally odd symmetry band structure obtained from density function theory (DFT) and experiment. The results of DFT theoretical calculation for surface (a) and bulk (b) of $MoS_2(0001)$ respectively are compared to the display of the experimental band structure obtained from angle resolved photoemission spectroscopy, for the s-polarization geometry and 34 eV photon energy along the $\overline{\Gamma}$ - $\overline{K}$ line. The direct comparison is made on (d) with the DFT theoretical calculations overlapped with experimental results shown in (a), (b) and (c), with blue dots for surface states from (a), and white dots for bulk band states from (b).

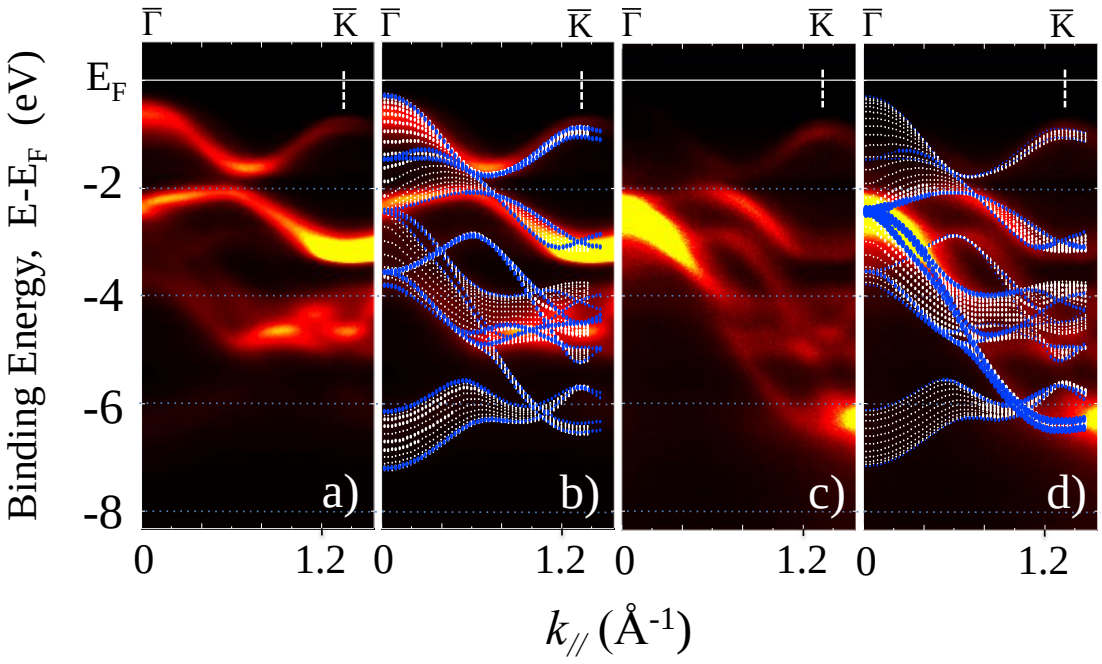

Figure 7-4: Comparison of both the nominally even (a,b) and odd (c,d) symmetry band structure (this assumes mirror plane symmetry along the $\overline{\Gamma}$ - $\overline{K}$ line is preserved) obtained from density function theory (DFT) and experiment. The results of DFT theoretical calculation for surface and bulk of MoS_2(0001) are compared to the experimental band mapping obtained for the p-polarization geometry (b), nominally even state and the s-polarization geomtry (d), nominally odd states. The experiment is derived from angle resolved photoemission spectroscopy results taken at 75 eV photon energy along the $\overline{\Gamma}$ - $\overline{K}$ line. In the comparison, the blue dots are for surface states from (Figure 7-2a, Figure 7-3a), and white dots for bulk band states from DFT theoretical calculations (Figure 7-2b, Figure 7-3).

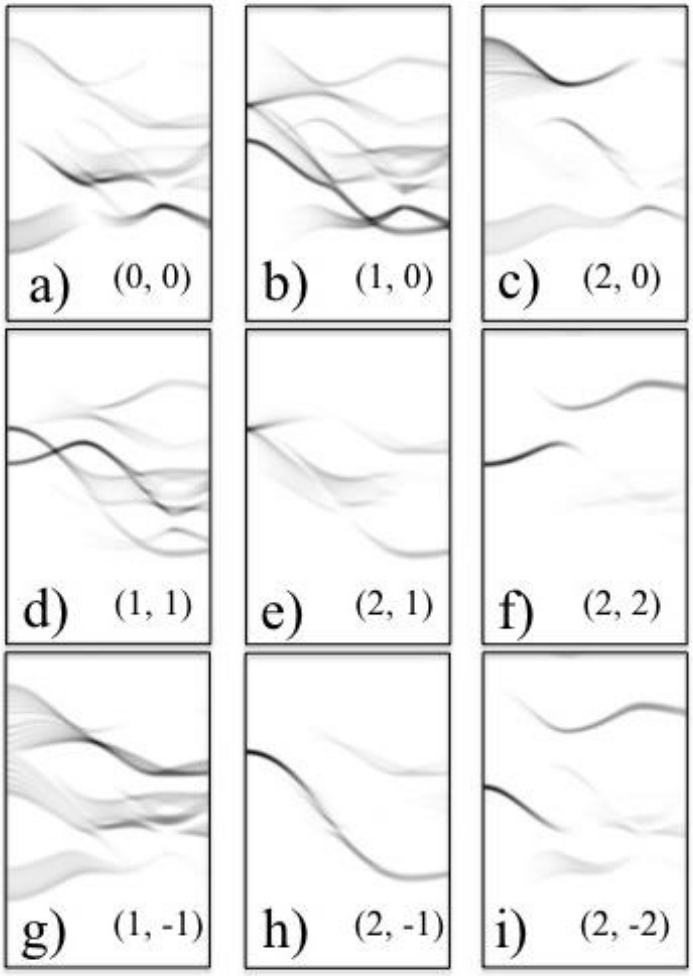

Figure 7-5: The calculated density functional theory of the state contributions to the $MoS_2(0001)$ band structure. The calculations are for the surface weighted states of $MoS_2(0001)$ according to azimuthal and polar quantum numbers i.e. the angular momentum and magnetic quantum numbers l and m, as indicated for each panel a) – i), by (l, m). These contributions permit some assignment of spectral weight character to the experimental band structure (see text). From the point of view of symmetry a) – f) are even states, and g) – i) are odd states.

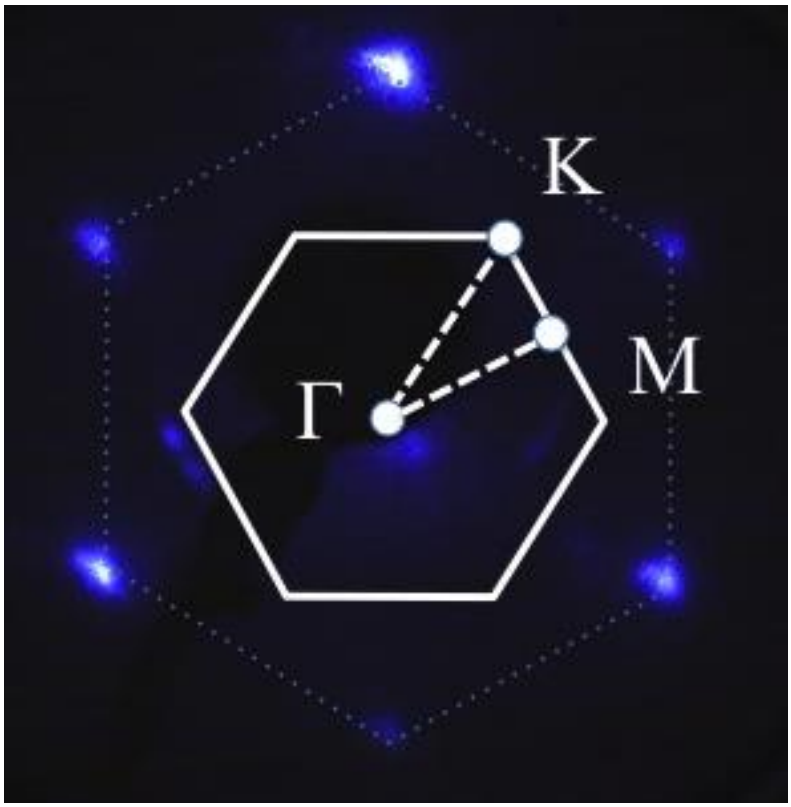

Figure 7-6: The surface Brillouin zone of the MoS_2(0001) surface overlaid on the low energy electron diffraction (LEED), taken at an incident electron energy (b) 101 eV. The critical points ($\overline{\Gamma}$, $\overline{M}$, $\overline{K}$) of the 2-dimensional surface Brillouin zone are illustrated, but important is that the line $\overline{\Gamma}$ to $\overline{K}$ has lost the mirror plane symmetry upon reduction of the applicable point group symmetry were C_{6v} to C_{3v}.

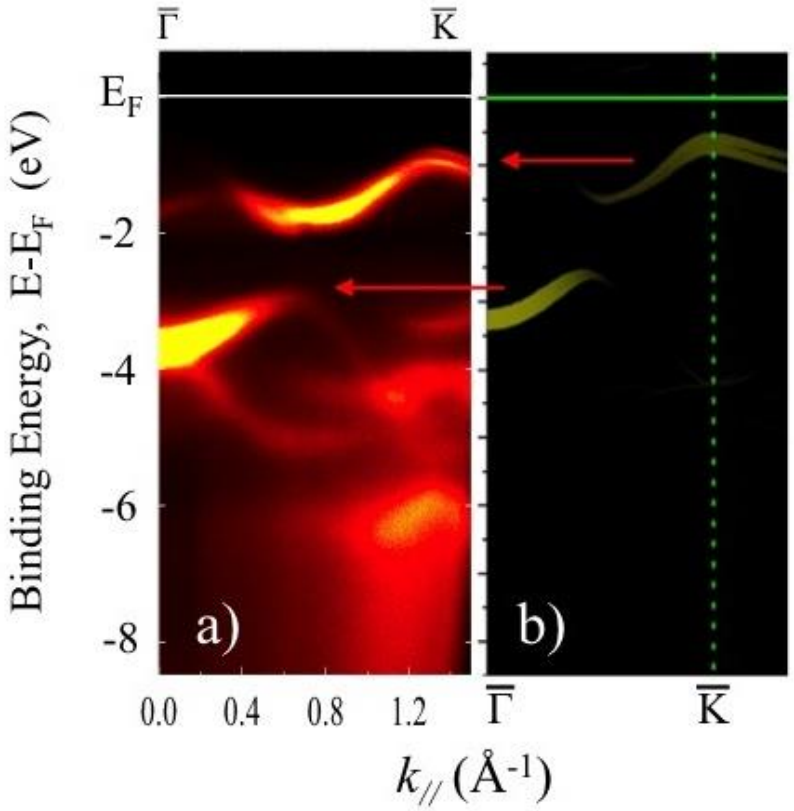

Figure 7-7: Comparison of the nominally odd symmetry band structure obtained from angle resolved photoemission spectroscopy, for the s-polarization geometry and 34 eV photon energy along the $\overline{\Gamma}$-$\overline{K}$ line. The direct comparison is made with the DFT theoretical band structure for the Mo $4d_{x}2\text{-}_{y}2$ (l=2, m=2) state alone.

Chapter 8 Summary

8.1 Summary

The XPS is a very surface sensitive analysis tool. We can investigate the composition, chemical environment and thickness of thin films or surface layers. We have shown that sputtering with low-energy argon ions is a method sufficiently mild to desulfurize monolayer MoS_2 while allowing its structural composition. In combinations, our findings suggest that low energy Argon sputtering may have significant potential in activation, attachment to and modification of MoS_2 layers

This simple procedure of tuning the bandgap of single-layer TMD films after growth suggests new research directions. Local attending of the bandgap should be possible by control of the sputtered region of the film. This would provide a means to produce heterojunctions and spatial variations of the bandgap for other purposes. At the same time, this study shows that induced strain in the film may also play an important role, providing another route for control of the bandgap.

Using CVD method, we can grow alloy monolayer films of $MoS_{2(1-x)}Se_{2x}$ of arbitrary composition through control of the S/Se ratio of the organic precursors used in the growth process. Photoluminescence, Raman, and AFM measurements show a high degree of homogeneity of the films, and theoretical studies strongly support the stability of the alloy films against phase separation. The band structure of the alloy films can be tuned continuously with composition, and both the experimental and theoretical studies show that the material exhibits a direct gap for

all alloy compositions. The room temperature optical bandgap is found to vary smoothly between the limits of 1.87 eV (for pure single-layer MoS_2) and 1.55 eV (for pure single-layer $MoSe_2$).

8.2 Future Work

For the thin film characterizations, future studies will explore the temperature dependence of the PL at lower temperatures and for bilayer material, where also trion peaks and coexistence of indirect bandgap PL can be found.

Using STM is an effective way to directly observe the detail information after the gentle Argon ion sputtering process. Although in situ MoS_2 STM images are obtained on Cu(111) surface, the defects of monolayer MoS_2 and Cu-S are comparable with the similar sputtering condition of MoS_2 on SiO_2 substrate.

Since the postgrowth modification will tune the chemical and electrical properties of the thin film, next step would address the electrical transport measurement of various sputtering conditions and of different compositions. The TPD experiments of different molecules will also be an important method for the catalytic analysis of modified TMD films.

Reference

1. Lin, M.W., et al., *Room-temperature high on/off ratio in suspended graphene nanoribbon field-effect transistors.* Nanotechnology, 2011. **22**(26).
2. Han, M.Y., et al., *Energy band-gap engineering of graphene nanoribbons.* Physical Review Letters, 2007. **98**(20).
3. Balog, R., et al., *Bandgap opening in graphene induced by patterned hydrogen adsorption.* Nature Materials, 2010. **9**(4): p. 315-319.
4. Mak, K.F., et al., *Atomically Thin MoS2: A New Direct-Gap Semiconductor.* Physical Review Letters, 2010. **105**(13).
5. Ma, Q., et al., *Controlled argon beam-induced desulfurization of monolayer molybdenum disulfide.* Journal of Physics-Condensed Matter, 2013. **25**(25).
6. Ma, Q., et al., *Postgrowth Tuning of the Bandgap of Single-Layer Molybdenum Disulfide Films by Sulfur/Selenium Exchange.* Acs Nano, 2014. **8**(5): p. 4672-4677.
7. Dwight, D.W., *Multiphoton, Monochromatic X-Ray Source for Xps.* Surface and Interface Analysis, 1986. **9**(1-6): p. 74-74.
8. *X-ray photoelectron spectroscopy; an introduction to principles and practices.* Sci-Tech News, 2012. **66**(3): p. 45-45.
9. Pacey, D.J., *Measurement of Vacuum.* Instrumentation Reference Book, 4th Edition, 2010: p. 165-173.
10. Redhead, P.A., *Citation Classic - Thermal-Desorption of Gases.* Current Contents/Engineering Technology & Applied Sciences, 1980(36): p. 16-16.
11. Mann, J., et al., *Facile growth of monolayer MoS2 film areas on SiO2.* The European Physical Journal B, 2013. **86**(5): p. 1-4.
12. Zhan, Y., et al., *Large-Area Vapor-Phase Growth and Characterization of MoS2 Atomic Layers on a SiO2 Substrate.* Small, 2012. **8**(7): p. 966-971.
13. Zande, A.M.v.d., et al., *Grains and grain boundaries in highly crystalline monolayer molybdenum disulfide.* arXiV, 2013. **1301.**1985.
14. Mak, K.F., et al., *Atomically Thin MoS_{2}: A New Direct-Gap Semiconductor.* PHYSICAL REVIEW LETTERS, 2010. **105**(13): p. 136805.
15. Kresse, G. and J. Furthmüller, *Efficiency of ab-initio total energy calculations for metals and semiconductors using a plane-wave basis set.* Computational Materials Science, 1996. **6**(1): p. 15-50.
16. Kresse, G. and J. Hafner, *Ab initio molecular dynamics for liquid metals.* Physical Review B, 1993. **47**(1): p. 558-561.
17. Press, W.H., *Numerical recipes : the art of scientific computing*. 3rd ed. 2007, Cambridge, UK ; New York: Cambridge University Press. xxi, 1235 p.
18. Perdew, J.P., K. Burke, and M. Ernzerhof, *Generalized Gradient Approximation Made Simple.* Physical Review Letters, 1996. **77**(18): p. 3865-3868.
19. Nose, S., *A unified formulation of the constant temperature molecular dynamics methods.* The Journal of Chemical Physics, 1984. **81**(1): p. 511-519.
20. Tongay, S., et al., *Thermally Driven Crossover from Indirect toward Direct Bandgap in 2D Semiconductors: MoSe2 versus MoS2.* Nano Letters, 2012. **12**(11): p. 5576-5580.

21. Butler, S.Z., et al., *Progress, Challenges, and Opportunities in Two-Dimensional Materials Beyond Graphene.* Acs Nano, 2013. **7**(4): p. 2898-2926.
22. Chhowalla, M., et al., *The chemistry of two-dimensional layered transition metal dichalcogenide nanosheets.* Nature Chemistry, 2013. **5**(4): p. 263-275.
23. Wang, Q.H., et al., *Electronics and optoelectronics of two-dimensional transition metal dichalcogenides.* Nature Nanotechnology, 2012. **7**(11): p. 699-712.
24. Sercombe, D., et al., *Optical investigation of the natural electron doping in thin MoS2 films deposited on dielectric substrates.* Sci. Rep., 2013. **3**.
25. Eda, G., et al., *Photoluminescence from Chemically Exfoliated MoS2.* Nano Letters, 2011. **11**(12): p. 5111-5116.
26. Ji, Q., et al., *Epitaxial Monolayer MoS2 on Mica with Novel Photoluminescence.* NANO LETTERS, 2013. **13**(8): p. 3870-3877.
27. Mann, J., et al., *2-Dimensional Transition Metal Dichalcogenides with Tunable Direct Band Gaps: $MoS_{2(1-x)}Se_{2x}$ Monolayers.* Advanced Materials, 2013: p. DOI: 10.1002/adma.201304389.
28. Mann, J., et al., *Facile Growth of Sub-Millimeter Scale Monolayer MoS2 Films on SiO2/Si.* European Physical Journal B, 2013. **86**: p. 226.
29. Plechinger, G., et al., *Low-temperature photoluminescence of oxide-covered single-layer MoS2.* physica status solidi (RRL) – Rapid Research Letters, 2012. **6**(3): p. 126-128.
30. Korn, T., et al., *Low-temperature photocarrier dynamics in monolayer MoS2.* Applied Physics Letters, 2011. **99**(10).
31. Besenbacher, F., et al., *Recent STM, DFT and HAADF-STEM studies of sulfide-based hydrotreating catalysts: Insight into mechanistic, structural and particle size effects.* Catalysis Today, 2008. **130**(1): p. 86-96.
32. Kang, J., et al., *Monolayer semiconducting transition metal dichalcogenide alloys: Stability and band bowing.* Journal of Applied Physics, 2013. **113**(14)
33. Komsa, H.P. and A.V. Krasheninnikov, *Two-Dimensional Transition Metal Dichalcogenide Alloys: Stability and Electronic Properties.* Journal of Physical Chemistry Letters, 2012. **3**(23): p. 3652-3656.
34. Lee, Y.-H., et al., *Synthesis of Large-Area MoS2 Atomic Layers with Chemical Vapor Deposition.* Advanced Materials, 2012. **24**(17): p. 2320-2325.
35. Najmaei, S., et al., *Vapour phase growth and grain boundary structure of molybdenum disulphide atomic layers.* Nat Mater, 2013. **12**(8): p. 754-759.
36. Yun, W.S., et al., *Thickness and strain effects on electronic structures of transition metal dichalcogenides: 2H-MX2 semiconductors (M = Mo, W; X = S, Se, Te).* Physical Review B, 2012. **85**(3): p. 033305.
37. Lu, P., et al., *Strain-dependent electronic and magnetic properties of MoS2 monolayer, bilayer, nanoribbons and nanotubes.* Physical Chemistry Chemical Physics, 2012. **14**(37): p. 13035-13040.
38. Mann, J., et al., *2-dimensional transition metal dichalcogenides with tunable direct band gaps: MoS(2)((1)-x) Se(2)x monolayers.* Adv Mater, 2014. **26**(9): p. 1399-404.
39. Li, H., et al., *Growth of alloy MoS(2x)Se2(1-x) nanosheets with fully tunable chemical compositions and optical properties.* J Am Chem Soc, 2014. **136**(10): p. 3756-9.

40. Lee, Y.-H., et al., *Synthesis of Large-Area MoS_2 Atomic Layers with Chemical Vapor Deposition.* Advanced materials, 2012. **24**: p. 2320-2325.
41. Zande, A.M.v.d., et al., *Grains and grain boundaries in highly crystalline monolayer molybdenum disulfide.* Nature Materials, 2013. **12**: p. 554–561.
42. Yifei Yu, et al., *Controlled Scalable Synthesis of Uniform, High-Quality Monolayer and Few-layer MoS_2 Films.* Scientific Reports, 2013. **3**: p. 1866.
43. Sina Najmaei, et al., *Vapour phase growth and grain boundary structure of molybdenum disulphide atomic layers.* Nature Materials, 2013.
44. Castellanos-Gomez, A., et al., *Laser-Thinning of MoS2: On Demand Generation of a Single-Layer Semiconductor.* Nano Letters, 2012. **12**(6): p. 3187-3192.
45. Liu, Y., et al., *Layer-by-Layer Thinning of MoS2 by Plasma.* Acs Nano, 2013.
46. O'Neill, A., U. Khan, and J.N. Coleman, *Preparation of High Concentration Dispersions of Exfoliated MoS2 with Increased Flake Size.* Chemistry of Materials, 2012. **24**(12): p. 2414-2421.
47. Zeng, Z., et al., *Single-Layer Semiconducting Nanosheets: High-Yield Preparation and Device Fabrication.* Angewandte Chemie International Edition, 2011. **50**(47): p. 11093-11097.
48. Lee, K., et al., *Electrical Characteristics of Molybdenum Disulfide Flakes Produced by Liquid Exfoliation.* Advanced Materils, 2011. **23**(36): p. 4178-4182.
49. Shi, Y., et al., *van der Waals Epitaxy of MoS2 Layers Using Graphene As Growth Templates.* Nano Letters, 2012. **12**(6): p. 2784-2791.
50. Liu, K.-K., et al., *Growth of Large-Area and Highly Crystalline MoS2 Thin Layers on Insulating Substrates.* Nano Letters, 2012. **12**(3): p. 1538-1544.
51. Boscher, N.D., et al., *Atmospheric pressure CVD of molybdenum diselenide films on glass.* Chemical Vapor Deposition, 2006. **12**(11): p. 692-698.
52. Mann, J., et al., *Facile Growth of Sub-Millimeter Scale Monolayer MoS2 Films on SiO2/Si.* European Physical Journal B, 2012.
53. Kang, J., et al., *Band offsets and heterostructures of two-dimensional semiconductors.* Applied Physics Letters, 2013. **102**(1).
54. Kresse, G. and J. Furthmüller, *Efficiency of ab-initio total energy calculations for metals and semiconductors using a plane-wave basis set.* Comput. Mat. Sci., 1996. **6**: p. 15.
55. Togo, A., F. Oba, and I. Tanaka, *First-principles calculations of the ferroelastic transition between rutile-type and CaCl(2)-type SiO(2) at high pressures.* Physical Review B, 2008. **78**(13): p. 134106
56. Zande, A.M.v.d., et al., *Grains and grain boundaries in highly crystalline monolayer molybdenum disulfide.* Nature Materials, 2012.
57. Odonnell, K.P. and X. Chen, *Temperature-Dependence of Semiconductor Band-Gaps.* Applied Physics Letters, 1991. **58**(25): p. 2924-2926.
58. Tongay, S., et al., *Thermally Driven Crossover from Indirect toward Direct Bandgap in 2D Semiconductors: MoSe2 versus MoS2.* Nano Letters, 2012. **12**(11): p. 5576-5580.
59. Dumcenco, D.O., et al., *Raman study of 2H-Mo1−xWxS2 layered mixed crystals.* Journal of Alloys and Compounds, 2010. **506**(2): p. 940-943.
60. Lee, Y.-H., et al., *Synthesis of Large-Area MoS2 Atomic Layers with Chemical Vapor*

Deposition. Advanced Materials, 2012: p. n/a-n/a.
61. NIST, *X-ray Photoelectron Spectroscopy Database*. 1989, National Institute of Standards and Technology: Gaithersburg, MD.
62. Balendhran, S., et al., *Atomically thin layers of MoS2via a two step thermal evaporation-exfoliation method.* Nanoscale, 2012. **4**(2): p. 461-466.
63. Lee, C., et al., *Anomalous Lattice Vibrations of Single- and Few-Layer MoS2.* Acs Nano, 2010. **4**(5): p. 2695-2700.
64. Splendiani, A., et al., *Emerging Photoluminescence in Monolayer MoS2.* Nano Letters, 2010. **10**(4): p. 1271-1275.
65. RadisavljevicB, et al., *Single-layer MoS2 transistors.* Nat Nano, 2011. **6**(3): p. 147-150.
66. Ghatak, S., A.N. Pal, and A. Ghosh, *Nature of Electronic States in Atomically Thin MoS2 Field-Effect Transistors.* Acs Nano, 2011. **5**(10): p. 7707-7712.
67. Late, D.J., et al., *Hysteresis in Single-Layer MoS2 Field Effect Transistors.* Acs Nano, 2012. **6**(6): p. 5635-5641.
68. Li, H., et al., *Fabrication of Single- and Multilayer MoS2 Film-Based Field-Effect Transistors for Sensing NO at Room Temperature.* Small, 2012. **8**(1): p. 63-67.
69. Yin, Z., et al., *Single-Layer MoS2 Phototransistors.* Acs Nano, 2011. **6**(1): p. 74-80.
70. Ayari, A., et al., *Realization and electrical characterization of ultrathin crystals of layered transition-metal dichalcogenides.* Journal of Applied Physics, 2007. **101**(1): p. 014507-5.
71. Edmondso.Dr, *Electronic Band-Structure of Layer-Type Crystal 2h-Mos2.* Solid State Communications, 1972. **10**(11): p. 1085-&.
72. Yun, W.S., et al., *Thickness and strain effects on electronic structures of transition metal dichalcogenides: 2H-M X-2 semiconductors (M = Mo, W; X = S, Se, Te).* Physical Review B, 2012. **85**(3).
73. Takeda, Y., et al., *High-resolution and low-temperature photoemission study of a Kondo insulator.* Journal of Electron Spectroscopy and Related Phenomena, 1998. **88**: p. 391-394.
74. Fukutani, K., et al., *New view of the occupied band structure of Mo(112).* Physical Review B, 2012. **85**(15).
75. Blochl, P.E., *Projector Augmented-Wave Method.* Physical Review B, 1994. **50**(24): p. 17953-17979.
76. Kresse, G. and D. Joubert, *From ultrasoft pseudopotentials to the projector augmented-wave method.* Physical Review B, 1999. **59**(3): p. 1758-1775.
77. Kresse, G. and J. Furthmuller, *Efficient iterative schemes for ab initio total-energy calculations using a plane-wave basis set.* Physical Review B, 1996. **54**(16): p. 11169-11186.
78. Kresse, G. and J. Hafner, *Ab-Initio Molecular-Dynamics Simulation of the Liquid-Metal Amorphous-Semiconductor Transition in Germanium.* Physical Review B, 1994. **49**(20): p. 14251-14269.
79. Coehoorn, R., et al., *Electronic-Structure of Mose2, Mos2, and Wse2 .1. Band-Structure Calculations and Photoelectron-Spectroscopy.* Physical Review B, 1987. **35**(12): p. 6195-6202.
80. Mahatha, S.K., K.D. Patel, and K.S.R. Menon, *Electronic structure investigation of*

MoS2 and MoSe2 using angle-resolved photoemission spectroscopy and ab initio band structure studies. Journal of Physics-Condensed Matter, 2012. **24**(47).

81. Jin, W.C., et al., *Direct Measurement of the Thickness-Dependent Electronic Band Structure of MoS2 Using Angle-Resolved Photoemission Spectroscopy.* Physical Review Letters, 2013. **111**(10).
82. Hermanson, J., *Final-State Symmetry and Polarization Effects in Angle-Resolved Photoemission Spectroscopy.* Solid State Communications, 1977. **22**(1): p. 9-11.